Monthly Notices of the ROYAL ASTRONOMICAL SOCIETY

MNRAS **528,** 796–814 (2024) https://doi.org/10.1093/mnras/stad3968
Advance Access publication 2023 December 22

On the identification of the first two young asteroid families in g-type non-linear secular resonances

V. Carruba [1,2★] S. Aljbaae [3,4] Z. Knežević [5] M. Mahlke [6] J. R. Masiero [7] F. Roig [8] R. C. Domingos [9] M. Huaman [10] A. Alves [1] B. S. Martins [1] G. Caritá [3] M. Lourenço [1] and S. C. Destouni [11]

[1] *São Paulo State University (UNESP), School of Natural Sciences and Engineering, Guaratinguetá, SP, 12516-410, Brazil*
[2] *Laboratório Interinstitucional de e-Astronomia - LIneA, RJ 20765-000, Brazil*
[3] *National Space Research Institute (INPE), Division of Space Mechanics and Control, C.P. 515, 12227-310, São José dos Campos, SP, Brazil*
[4] *Make The Way, R. Elvira Ferraz, 250 - FL Office 305 e 306 - Vila Olãmpia, São Paulo - SP, 04545-015, Brazil*
[5] *Serbian Academy of Sciences and Arts, 11000 Belgrade, R. Serbia*
[6] *Institut d'Astrophysique Spatiale, Université Paris-Saclay, CNRS, F-91405 Orsay, France*
[7] *Caltech/IPAC, Pasadena, CA 91125, USA*
[8] *Observatório Nacional/ON-COAST, Rio de Janeiro, RJ 20921, Brazil*
[9] *São Paulo State University (UNESP), São João da Boa Vista, SP, 13876-750, Brazil*
[10] *Universidad Tecnológica del Perú (UTP), Cercado de Lima, 15046, Perú*
[11] *Chalmers University of Technology, SE-412 96 Gothenburg, Sweden*

Accepted 2023 December 21. Received 2023 December 20; in original form 2023 December 6

ABSTRACT

Linear secular resonances happen when there is a commensurability between the precession frequency of the pericenter, g, or longitude of the node, s, of an asteroid and a planet. Non-linear resonances are higher order combinations of these frequencies. Here, we studied the three most diffusive g-type non-linear secular resonances using Artificial Neural Networks. We identified a population of more than 2100 resonant objects in the $g - 2g_6 + g_5$ and $g - 3g_6 + 2g_5$ resonances. This allows the creation of a Convolutional Neural Network model for the $g - 2g_6 + g_5$ resonance, able to predict the status of several thousands of asteroids in seconds. We identified 12 new possible dynamical groups among the resonant population, including the 5507 and 170776 families, which have both estimated ages of less than 7 Myr. These are the two first-ever identified young families in resonant configurations of the investigated resonances, which allows for setting limits on their original ejection velocity field.

Key words: astronomical data bases: miscellaneous – minor planets, asteroids: general – minor planets, asteroids: individual.

1 INTRODUCTION

Asteroid families are groups of asteroids that formed from collisions or rotational break-ups of a parent body. The orbits of family members evolve after the formation event because of the gravitational effects of planets and massive asteroids, or non-gravitational forces like the Yarkovsky effect (Bottke et al. 2001). Secular resonances are one of the main gravitational effects. Linear secular resonances occur when there is a commensurability between the precession frequency of the longitude of pericenter ϖ, indicated as g, or of the node, Ω, indicated as s, of a planet and an asteroid. The most diffusive linear secular resonance in the main belt is the $\nu_6 = g - g_6$ resonance, where the suffix 6 is associated with the planet Saturn. Non-linear secular resonances involve higher order commensurabilities of planets' and asteroids' frequencies. Their argument can also be identified in terms of linear secular resonances. For example, the z_K resonance series of both nodes and pericenter can be written as $z_K = K(g - g_6) + (s - s_6) = K\nu_6 + \nu_{16}$, $K = 1, 2, 3,...$, with $\nu_{16} = s - s_6$ being the linear secular resonance of node with Saturn. Resonances that only involve combinations of the g frequency are called g-type secular resonances. They only affect the eccentricity of asteroids interacting with them and can influence the dynamical evolution of large asteroid families, like Astraea (Milani et al. 2014, 2017).

The dynamic effects of all g-type resonances up to order six were recently studied in Huaman et al. (2017), which identified three resonances responsible for most of the dynamical dispersion of asteroid families: the $g - 2g_6 + g_5$, the $g - 3g_6 + 2g_5$, and the $2g - 3g_5 + g_6$. The suffix fifth stands for Jupiter, the fifth planet from the Sun. The $g - 2g_6 + g_5$ resonance is one of the most important non-linear secular resonances, crossing densely populated regions of the asteroid belt and affecting a large number of asteroid families, like Astraea. Its location was first obtained in Milani & Knežević (1990). Recently, Knežević (2022) mapped and identified the asteroid families that are crossed by this resonance. The $g - 3g_6 + 2g_5$ is notable for its interaction with the Koronis family that gives rise to the so-called Prometheus surge, a region of the Koronis family with higher eccentricity values than the rest of the group. The Prometheus surge was one of the arguments used in Bottke et al. (2001) to validate the importance of the Yarkovsky effect on the dynamical evolution of asteroid families affected by secular resonances.

★ E-mail: valerio.carruba@unesp.br

Table 1. The three most diffusive g-type secular resonances in the main belt, according to Huaman et al. (2017). We report the resonant argument in terms of frequencies, in terms of combinations of linear secular resonances, the central value of the asteroidal g frequency associated with each resonance, and the number of asteroids, numbered and multi-opposition, likely to be affected by the resonances.

Res. argument frequencies	Res. argument linear resonances	Frequency value (arcmin yr^{-1})	Numbered ast.	Multi-opp. ast
Fourth order:				
$g - 2g_6 + g_5$	$2\nu_6 - \nu_5$	52.229	15 267	6422
Sixth order:				
$g - 3g_6 + 2g_5$	$3\nu_6 - 2\nu_5$	76.215	1780	928
$2g - 3g_5 + g_6$	$3\nu_5 - \nu_6$	−7.736	15	7

Traditionally, after an initial phase by which possible resonant asteroids are identified based on their frequencies, the detection of a resonant asteroid is performed by a visual inspection of the behaviour of its resonant argument, i.e. the combination of the asteroid and planets angles associated with each resonance. For the $g - 2g_6 + g_5$, this would be the $\varpi - 2\varpi_6 + \varpi_5$ angle. The resonant argument of asteroids in librating states would oscillate around an equilibrium point, while for objects not in resonance it will circulate from 0° to 360° deg, or alternate phases of circulations and librations (the so-called switching orbits).

Currently, there are more than 1 million known asteroids, and a study of a single resonance may involve checking the status of several thousands of resonant arguments. This is already a vexing task for a human observer and things will considerably get worse when the 10-yr Rubin Observatory Legacy Survey of Space and Time (LSST) starts operations in 2025 (https://www.lsst.org/about/timeline). The catalogues created by the LSST, according to Jones, Jurić & Ivezić (2015), will increase the total number of small bodies in the Solar system that are known by a factor of 10–100 times, with $\simeq$ 1 million more asteroids expected to be discovered in the first year of operations alone. New methods for classifying large populations of likely resonant asteroids are needed to deal with the huge influx of expected new data. In Carruba et al. (2021), we introduced methods based on Artificial Neural Networks (ANN) to automatically classify images of asteroids' resonant arguments. More recently, Carruba et al. (2022a) used Convolutional Neural Networks (CNNs) and their optimizations, for classifying large images data bases. The main goal of this work is to obtain machine learning and deep learning models for g-type non-linear secular resonances, to more speedily classify the large new asteroidal population that is expected to be detected soon.

This can also allow interesting developments for asteroid families identifications. A new data set of asteroids in librating states of the $\nu_6 = g - g_6$ linear secular resonance were recently used in Carruba et al. (2022b) to identify the main asteroid families interacting with that resonance. As a result, the (12988) Tiffanykapler young asteroid family was identified as the first in a linear secular resonance. Here, we conduct a similar analysis for the new populations of likely resonators, so as to identify other possible families. Because of their relatively young age of 7 Myr or less, special numerical techniques based on time-reversal simulations can be used to date these asteroid families, providing exceptionally accurate age estimates, not available for older groups. Other techniques, based on the recognition of clusters of resonant asteroids in an appropriate space of orbital proper elements (Milani et al. 2017), are also used to characterize the newly identified families.

2 METHODS

As a first-pass criterion to locate asteroids within the g-type non-linear secular resonances, we apply the Carruba (2009) method. In that work, we identified the objects most likely to be in librating states as those for which $g + s = (g_6 + s_6) = \pm 0.2$ arcsec yr^{-1}, given the z_1 secular resonance of argument $z_1 = g - g_6 + s - s_6$. We think that this could be a reasonable criterion to identify objects likely to be in fourth- and sixth-order g-type non-linear secular resonances, because the breadth of the librating zone for asteroids in the fourth-order secular resonance tends to be less than this threshold (Carruba 2009). We used this criterion for all numbered asteroids with identifications up to 616 689 for which proper elements and frequencies, computed using the Knežević & Milani (2003) technique, also described in Carruba (2010), are available at the Asteroid Families Portal *AFP* ['http://asteroids.matf.bg.ac.rs/fam/index.php', Radović et al. (2017); Novaković et al. (2022), accessed on November 2022], or also at the AstDyS website ['https://newton.spacedys.com/astdys/' Knežević & Milani (2003)]. Finally, an additional 285 861 multi-opposition asteroids are also available at *AFP*. The source of proper elements and frequencies used in this work was only *AFP*. It is important to note that the overall effect of the secular resonances is to reduce orbital stability. Therefore, in this study, we have taken measures to enhance the reliability of our analysis by excluding highly chaotic objects with Lyapunov times of less than 100 yr, for which reliable values of synthetic proper elements, according to Knežević & Milani (2003), could not be obtained. These exclusions contribute to a more robust and focused investigation of the remaining asteroids within the study.

Up to sixth-order secular resonances, Huaman et al. (2017) pinpointed three prominent g-type resonances that exhibited significant dynamical effects on asteroid families. These resonances are denoted as $g - 2g_6 + g_5$, $g - 3g_6 + 2g_5$, and $2g - 3g_5 + g_6$. Table 1 provides details such as their names, central frequency values, and the counts of numbered and multi-opposition asteroids potentially influenced by these resonances. Currently, there are just 15 numbered asteroids that are potential librators of the $2g - 3g_5 + g_6$ resonance and none of them are librating. Since other g-type resonance tended to have a lesser effect on asteroid dynamical evolution, in this work we will concentrate our attention only on the $g - 2g_6 + g_5$ and the $g - 3g_6 + 2g_5$ resonances. Also, since resonant arguments are easier to remember if expressed as combinations of linear terms, from now on we will use the latter notation, i.e. $g - 2g_6 + g_5 = 2\nu_6 - \nu_5$, and $g - 3g_6 + 2g_5 = 3\nu_6 - 2\nu_5$.

To identify the population of resonant asteroids, we adopted the methodology outlined in Carruba et al. (2021). This approach relied on a basic feedforward ANN model, comprising a 'Flatten'

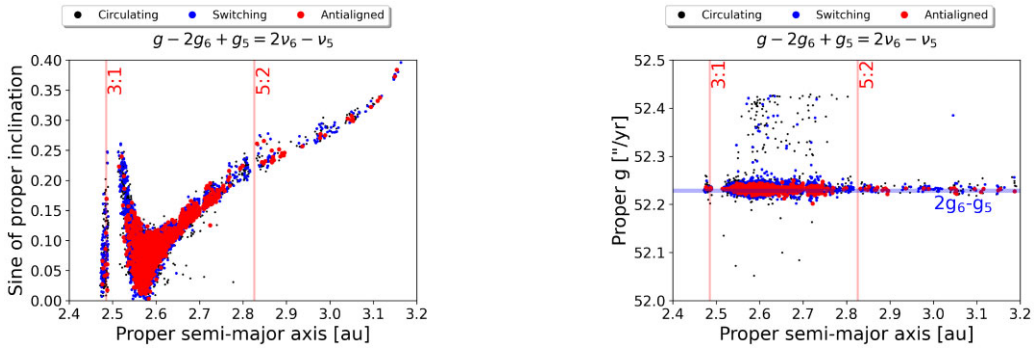

Figure 1. Left panel: A proper (a, $\sin(i)$) projection of asteroids in the $2\nu_6 - \nu_5$ resonance. Vertical lines display the location of the main mean-motion resonances in the area. Right panel: A proper (a, g) projection of the same asteroids, for asteroids with errors in proper g of less than 0.25 arcsec yr^{-1}. The horizontal line shows the center of the resonance. The legends in both panels identify the type of asteroid's orbits.

layer for data preparation, followed by two 'Dense' layers with ReLU activation for feature extraction, and a final 'Dense' layer with softmax activation for classifying asteroids into their respective resonant categories. This streamlined and automated process leveraged TensorFlow and Keras libraries for efficient implementation and training. The methodology followed a five-step procedure. First, asteroids underwent numerical integration under the gravitational influence of all planets for 10 million years. Cartesian vectors required for the SWIFT integrator were generated following the procedure described in section 2.8 of Murray & Dermott (1999). Notably, we omitted the inclusion of Ceres and massive asteroids in this stage, as their effects were deemed unnecessary for precisely determining secular resonance positions. Subsequently, images depicting the time evolution of the relevant resonant argument for each resonance were generated. The ANN perceptron model from Carruba et al. (2021) was then trained using labelled images in a training set, and predictions were made for a separate set of 50 test images. These predictions were subsequently validated through independent visual inspection conducted by multiple co-authors. Up to 15 per cent of the asteroids may be reclassified after the double-blind tests are conducted. The typical fraction of asteroids reclassified is usually approximately 5 per cent.

Finally, once the population of possible librating asteroids has been identified, we investigate the effect that non-gravitational forces can have on the permanence of asteroids in librating states. For this purpose, we follow the approach of Carruba et al. (2022b): two sets of orbital clones with maximum and minimum values of spin obliquities are created, and the YORP (Yarkovsky–O'Keefe–Radzievskii–Paddack) effect is neglected, to maximize the Yarkovsky drift in the semimajor axis. Maximizing the Yarkovsky drift allows us to explore extreme scenarios, where this effect has the most significant impact on an asteroid's orbit, aiding our comprehensive analysis of the dynamical behaviour of these objects. We use the set of physical parameters (density, bulk density, thermal conductivity, specific heat, and bond albedo) described in Carruba et al. (2022b), which also aims at maximizing the Yarkovsky drift, and the particles are integrated over 10 Myr over the influence of all planets, created two sets of clones, one with a spin obliquity of $+90^\circ$ and one with -90°. The time behaviour of the resonant argument is then verified for both clones, and if they are both in librating states, the asteroid is confirmed as a librator and is added to our sample for families' studies.

Results for the resonances of interest will be reported in the next subsections.

2.1 $2\nu_6 - \nu_5$ resonance

The results of simulations and *ANN* analysis identified 1517 numbered asteroids with available synthetic proper elements and 389 multi-opposition asteroids suspected to be in $2\nu_6 - \nu_5$ librating states. Simulations with the Yarkovsky force confirmed this status for 1337 numbered and 357 multi-opposition bodies, respectively.

The distribution of the identified asteroids in the proper (a, $\sin(i)$) and (a, g) planes is shown in Fig. 1. The great majority of the librating orbits are found near the centre of the resonance, as seen in the right panel of Fig. 1, which supports the validity of our analysis. Switching orbits are mostly encountered at the resonance boundary. Finally, most asteroids in the $2\nu_6 - \nu_5$ resonance are found in the central main belt, with a small tail in the outer belt. No resonant asteroids were encountered in the inner main belt.

2.2 $3\nu_6 - 2\nu_5$ resonance

We identified 1776 numbered asteroids with publicly available synthetic proper elements and 722 multi-opposition bodies possibly in the $3\nu_6 - 2\nu_5$ resonance. Regrettably, the time behaviour of librating resonant angles for this resonance is slightly different than that of the previously analysed $2\nu_6 - \nu_5$ resonance. Because of that, the previously trained ANN models perform poorly in classifying resonant arguments for this resonance, and models based on actual labels of the $3\nu_6 - 2\nu_5$ resonance are also not viable, since there are just too few asteroids (2498) to efficiently train an *ANN* model that usually requires tens of thousands of images. For this reason, we visually analysed the resonant arguments of the asteroids' candidates under the effect of the Yarkovsky force. This analysis confirmed the librating status for 132 numbered and 78 multi-opposition asteroids, respectively.

Fig. 2 shows the distribution of these objects the proper (a, $\sin(i)$) and (a, g) planes. Librating asteroids are only found in the outer main belt, and have values of proper g close to that of the resonance centre, $3g_6 - 2g_5 = 76.215$ arcmin yr^{-1}, as expected.

3 DEEP LEARNING MODELS OF g-TYPE RESONANCES

As seen in Section 2.1, the data base of images for the $2\nu_6 - \nu_5$ resonant argument was both large enough and reliable enough to sustain the use of more advanced image classification methods. This

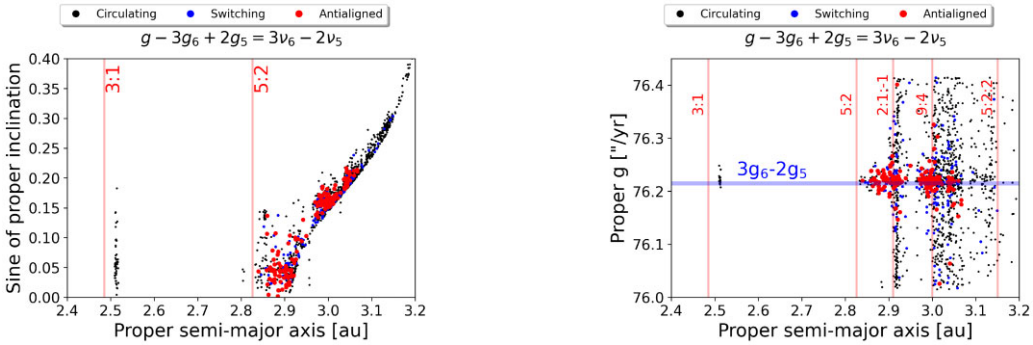

Figure 2. Left panel: A proper (a, $\sin(i)$) projection of asteroids in the $3\nu_6 - 2\nu_5$ resonance. Vertical lines display the location of the main mean-motion resonances in the area. Right panel: A proper (a, g) projection of the same asteroids. Symbols are the same as in Fig. 1.

study harnessed the power of CNN, Visual Geometry Group (VGG) model (Simonyan & Zisserman 2014), Inception (Szegedy et al. 2015), and ResNet He et al. (2015) models to explore the new $2\nu_6 - \nu_5$ data base. In order to ensure the robustness of the models, a comprehensive methodology was followed.

The data set was divided into three distinct parts:

(i) Training set: This segment of the data set was designated for the primary purpose of training the models. It served as the foundation upon which the models learned intricate patterns and relationships within the data. These patterns allowed the models to recognize and classify images effectively.

(ii) Validation set: A separate portion of the data set was set aside for validation purposes. This validation set played a critical role in assessing the models during their training process. It allowed for continuous evaluation of their performance and helped fine-tune various parameters. The validation set served as a quality control mechanism, ensuring that the models were not overfitting the training data.

(iii) Test set: To gauge the models' generalization capabilities and behaviour on external data, a distinct and independent test data set was created. This data set was never seen by the models during their training or validation phases. Instead, it provided a real-world assessment of how well the models could make predictions on new, unseen images.

To enhance the models' performance and prevent overfitting, various regularization techniques were judiciously applied. These techniques included data augmentation (DA), dropout (DO), and batch normalization (BN). By employing these regularization strategies, the models were able to maintain their ability to generalize effectively to new, unseen data, ultimately resulting in more reliable and accurate predictions. More details on these practices can be found in Carruba et al. (2022a).

Our models are based on CNNs: CNNs are a class of deep neural networks designed to autonomously learn patterns, features, and hierarchical structures from input images. Unlike our basic ANN, CNNs incorporate convolutional layers that efficiently capture local patterns through filter applications. CNNs feature deeper and more complex architectures, with each layer extracting increasingly higher level features.

VGG model (Visual Geometry Group network): VGG model is another deep convolutional neural network architecture renowned for its simplicity and effectiveness. VGG model networks consist of convolutional layers followed by max-pooling layers, resulting in a straightforward and uniform structure. Compared to our basic ANN, VGG model is significantly deeper and excels at capturing abstract and complex image features. However, this depth requires increased computational resources, making VGG model ideal for tasks prioritizing accuracy over computational efficiency.

Table 2. Execution time, memory, maximum memory allocation, best epoch, and best accuracy for the models tested in this work for the $2\nu_6 - \nu_5$ data base using an 11th Gen Intel(R) Core(TM) i7-11700F @ 2.50GHz CPU. Memory allocations are measured in gigabytes (GB).

Model	Time (h:m:s)	Memory alloc. (GB)	Max. memory alloc. (GB)	Accuracy
VGG model	1:00:51.6	1.33	3.08	0.50
Inception	1:22:36.1	1.22	3.08	0.73
ResNet	0:40:51.4	1.22	3.08	0.70

ResNet (Residual Network): ResNet represents a breakthrough in deep learning by addressing the challenge of training extremely deep neural networks. It introduces residual blocks and skip connections, enabling the training of exceptionally deep networks while mitigating the vanishing gradient problem.

Inception: The Inception model is a deep learning architecture designed to capture features at various scales and dimensions within images. It employs complex structures called 'inception modules' for efficient feature extraction. Compared to our basic ANN, inception excels at handling complex data sets with intricate patterns and relationships. It is important to note that Inception is not the same as the basic ANN discussed earlier. Instead, it is a deeper and more powerful neural network architecture.

The evaluation of model performance was based on the 'accuracy' and 'F-beta' measures. 'Accuracy' represents the proportion of correctly predicted labels, while 'F-beta' is a composite score considering both 'Precision' (correctly predicted labels for the positive class) and 'Recall' (correctly predicted labels for the positive class out of all potentially positive predictions). Further details regarding these metrics and the selection of the best-performing CNN model can be found in Carruba et al. (2022a).

In this analysis, we applied the same methodologies to a data set of images representing the $2\nu_6 - \nu_5$ resonant arguments. The data set was partitioned into three subsets: 13 052 images for training (comprising all numbered asteroids up to designation 523 134), 2108 images for validation (encompassing all numbered asteroids with designations between 523 134 and 600 000), and 71 asteroids for the test set (consisting of numbered asteroids with designations greater than 600 000). A summary of our results is presented in Table 2.

We note that, among the models considered, the Inception model emerged as the top performer, followed by the ResNet and VGG

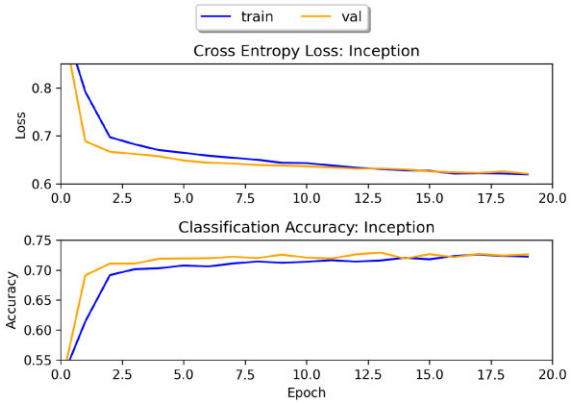

Figure 3. Dependence of *cross-entropy loss* and *accuracy* as a function of the model epoch for the $2\nu_6 - \nu_5$ best-performing CNN model.

models. To address the overfitting phenomenon, we applied a Dropout layer with a rate of 0.4 to each model, along with Ftrl optimization. Fig. 3 illustrates the performance behaviour of the Inception model, showing the trends in both cross-entropy loss (as defined in Carruba et al. 2022a, equation 3) and accuracy.

Notably, the cross-entropy loss of the validation set exhibits a decrease, while accuracy increases with each epoch. However, it is crucial to highlight that the model's significant learning appears to plateau after five epochs. This observation implies that beyond the fifth training iteration, the model has essentially converged to a solution, with further training iterations not yielding marginal improvements.

As previously mentioned, in addition to the conventional practice of utilizing a dedicated validation data set for evaluating the model's performance on unseen data during training, we extended our assessment to include external data sources. This comprehensive evaluation provides valuable insights into the model's generalization capabilities and behaviour when confronted with data beyond the boundaries of the training and validation sets.

4 IDENTIFICATION OF ASTEROID GROUPS INTERACTING WITH *g*-TYPE SECULAR RESONANCES

Asteroid families interacts with secular resonances in different way. While there are cases of families for which all the members are in resonant configurations, like the Tina (Carruba & Morbidelli 2011) and Tiffanykapler (Carruba et al. 2022b) families in the ν_6 secular resonance, or the Zelima sub-family (Tsirvoulis 2019) in the z_1 non-linear secular resonance, most asteroid families that interacts with linear or non-linear secular resonances have just a fraction of their members in resonant configurations, like the Padua family in the z_1 resonance (Carruba 2009).

The identification of substructures of large asteroid families that are in resonant configurations may be difficult. Small sub-families in large, dense families could be difficult to detect using standard methods, or, if detected, their dynamical importance could not be perceived by researchers not aware of their resonant status. Here, we plan to use the methods applied in Carruba et al. (2022b) to identify dynamical groups interacting with the $2\nu_6 - \nu_5$ and $3\nu_6 - 2\nu_5$ resonances. These are not necessarily independent asteroid families, but could either be (i) part of larger families interacting with the two secular resonances, or (ii) sub-families or secondary families formed in recent impacts. The latter cases will be investigated using time-reversal numerical methods later on in this paper.

Since the early 1990s, asteroid families have been identified using the Hierarchical Clustering Method (HCM) (Zappala et al. 1990; Bendjoya & Zappalà 2002). The most popular version of the approach uses a distance metric suited for the given task to search for an asteroid's neighbours in a domain of the $(a, e, \sin(i))$ proper elements. The second asteroid is added to the family member list if the distance between the first and second asteroids is less than a critical value, d_0, and the process is then repeated for the second body until no more bodies are detected. The method's free parameter, d_0, is based on the density of asteroids in a certain orbital zone. In this case, we use the strategy described in Beaugé & Roig (2001), which defines d_0 as the average of the lowest distances between all asteroids in the area.

Determining family membership versus cut-off and using stalactite diagrams are two effective techniques for detecting asteroid families. With the first approach, one displays the number of family members as a function of increasing distances, up to values of distances that are so great that every asteroid in the orbital zone belongs to a certain family. The asteroids in a family that comprises all the objects in the area are first depicted in a stalactite diagram, as, for instance, shown in Brož & Vokrouhlický (2008). After lowering the cut-off distance value, asteroid groupings are found within the population of objects that are no longer connected to the original family. The process is then repeated for decreasing distance cut-off values. The results are depicted in a plane with the distance cut-off on the y-axis and the memberships of the families on the x-axis. See Carruba (2010) for further information on each of these steps and processes.

Families determined with this approach can then be tested in an extended proper element data base including all asteroids in the regions, to see how quickly they may merge with other local families, as listed in surveys like those of Nesvorný, Brož & Carruba (2015) and Milani et al. (2014). Finally, machine learning methods optimized by the use of genetic algorithms can be used to attach multi-opposition asteroids to the core families identified among the numbered population of librating bodies. Interested readers can find more details about both these approaches in Carruba et al. (2022b).

4.1 $2\nu_6 - \nu_5$ resonance: families identification

Asteroids in librating states of the $2\nu_6 - \nu_5$ resonance are mostly located in the central belt, with a few scattered asteroids in the outer main belt. We identified 1337 asteroids in the central main belt, and 21 in the outer one. We first applied HCM and the stalactite diagram method to the two data bases and plots of the dependence of the number of family members as a function of the velocity cutoff are shown in Fig. 4. The value of d_0 was 100.5 m s^{-1} in the central main belt, and 407.0 m s^{-1} in the outer belt. In the central main belt, almost all asteroids are connected to the main 2198 Ceplecha initial body at a cut-off of 200 m s^{-1}, while this happens in the outer main belt at a cut-off of 500 m s^{-1}. Several different clusters are observed in the central main belt, while only one is detectable in the outer main belt, that of (47883) 2000 FZ$_{39}$. To analyse the librating population in the central main belt, we use the stalactite approach outlined in Section 4.

Our results are shown in the left panel of Fig. 5 and summarized in Table 3. Overall, we identified eight different asteroid groups, whose orbital distribution in the $(a, \sin(i))$ plane is displayed in the right panel of Fig. 5. All these groups are made of subpopulations of resonant asteroids of the Astraea family, which is well known for its interaction with the $2\nu_6 - \nu_5$ secular resonance (Milani et al. 2014). The fifth column of Table 3 shows the value of the cut-off for which

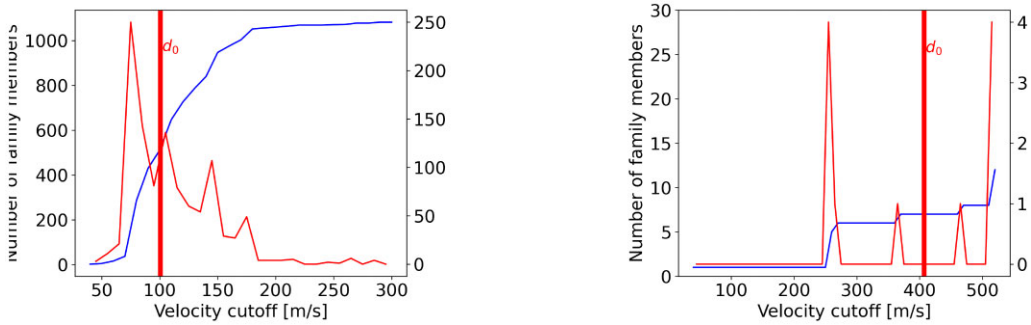

Figure 4. Left panel: Dependence of the number of asteroid family members (left y-axis), and of the incremental number of asteroid family members (right y-axis) on the HCM velocity cut-off for $2\nu_6 - \nu_5$ resonant asteroids in the central main belt. Right panel: The same, but for the outer belt.

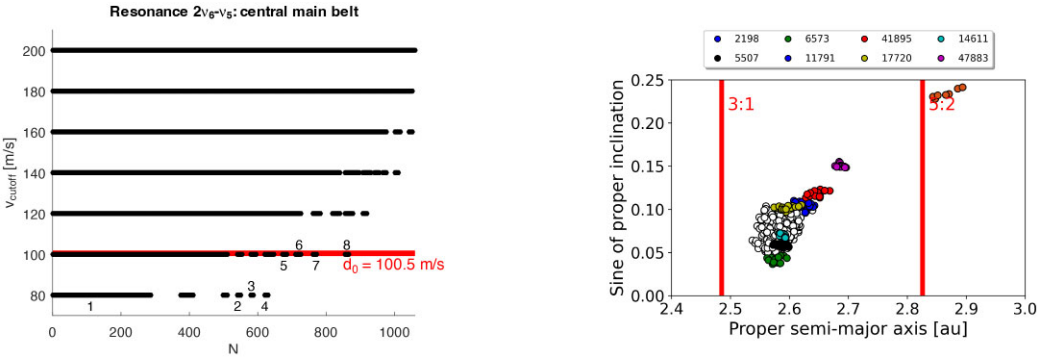

Figure 5. Left panel: A stalactite diagram for the asteroids in the $2\nu_6 - \nu_5$ resonance. The numbers on the plot identify the groups, according to the nomenclature of Table 3. Right panel: A proper (a, $\sin(i)$) distribution of the resonant asteroid groups identified in this work.

Table 3. Identification of the asteroid groups interacting with the $2\nu_6 - \nu_5$ secular resonance identified in this work. The fifth column displays the velocity cut-off for which the families join the Astraea family and in the last column the number of multi-opposition asteroids identified as possible family members by machine learning methods optimized through the use of genetic algorithms.

Group #	Asteroid id.	Asteroid name	Number of members	Velocity cut-off (m s^{-1})	# multi-opp. asteroids
1	2198	Ceplecha	511	70	110
2	5507	Niijima	14	60	0
3	6573	Magnitskij	16	80	0
4	11 791	Sofiyavarzar	27	80	13
5	41 895	(2000 WJ_{121})	13	90	0
6	17 200	(2000 AF_{47})	16	90	0
7	14 611	Elsaadawi	11	50	0
8	47 883	(2000 FZ_{39})	11	100	0

the groups join the Astraea large family. Using the machine learning methods optimized by the use of genetic algorithms, originally discussed in Carruba et al. (2022b), we identified a population of 110 multi-opposition asteroids that are connected to the 2198 group, and 13 multi-opposition bodies connected to the 11791 cluster. Their orbital distribution in the proper (a, $\sin(i)$) plane is shown in Fig. 6.

4.2 $3\nu_6 - 2\nu_5$ resonance

Resonant asteroids in the $3\nu_6 - 2\nu_5$ resonance are only located in the outer main belt, where we identified 170 numbered and 78 multiple opposition asteroids. The value of d_0 for the numbered resonant data set was 167.2 m s^{-1}. The dependence of the number of family members as a function of the velocity cut-off is shown in Fig. 7. We start with the lowest numbered object with a sizeable family in the region, 33 189 Ritzdorf, which is located in the pristine region of the main belt, near the Koronis family. The family grows larger, and it merges with other groups beyond the 9:4 mean-motion resonance with Jupiter for a cut-off of 750 m s^{-1}.

The right panel of Fig. 8 displays the results of an analysis using the stalactite approach. Properties of the identified groups are also summarized in Table 4. None of the identified groups are part of asteroid families as listed by Nesvorný, Brož & Carruba (2015) and Milani et al. (2014). However, the 33 189 group is very close to the Koronis asteroid family, and the other three groups are on the outskirts of the large Eos family. The possibility of these

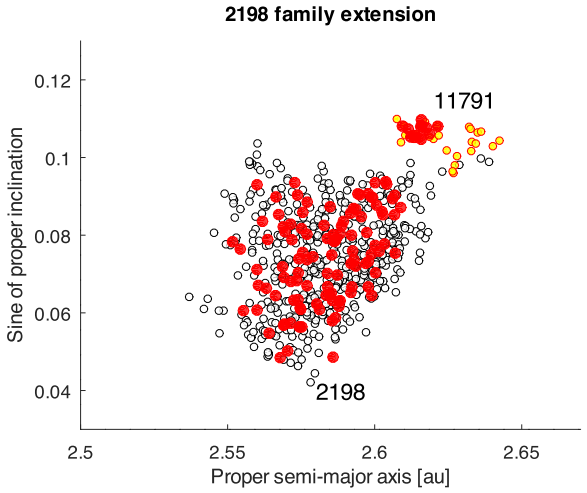

Figure 6. An $(a, \sin(i))$ projection of the numbered population of the 2198 and 11 791 groups (symbols are the same as in Fig. 5). The filled red circles show the location of the extended population among multi-opposition asteroids for the two clusters.

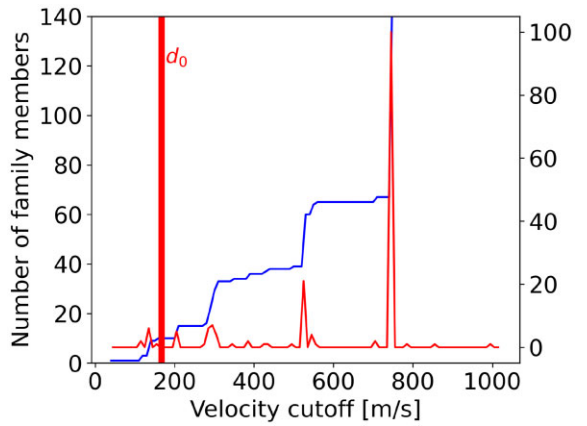

Figure 7. Dependence of the number of asteroid family members (left y-axis), and of the incremental number of asteroid family members (right y-axis) on the HCM velocity cutoff for $3\nu_6 - 2\nu_5$ resonant asteroids in the outer main belt.

groups belonging to the halos of the Koronis and Eos families, as defined in Brož & Morbidelli (2013), will be further investigated later on in this paper. The fifth column of Table 4 reports the values of the cut-offs for which the groups merge with the two families. Finally, machine learning methods optimized by genetic algorithms identified multiple-opposition asteroids connected to the 33189, 233054, and 97 217 groups. Their proper $(a, \sin(i))$ orbital distribution is displayed in Fig. 9.

5 PHYSICAL PROPERTIES OF THE NEW GROUPS

As asteroid families form from the break-up of a larger parent body, they are expected to have consistent compositions across family members. Physical property information such as albedo (Masiero et al. 2013), colours (Parker et al. 2008) or both (Carruba et al. 2013) can be used to improve family membership lists by removing potential background contaminants and reducing confusion when searching for additional family members. In this section, we consolidate the information from public data bases that are available for members of the asteroid groups identified in this work. First, we compare the physical properties of the family members to that of the family background population, which we define as a region that includes all objects, numbered and multi-oppositions, within $\pm5^\circ$ of proper inclination, ±0.05 proper eccentricity, and ±0.05 au of proper semimajor axis [with cut-offs at the major mean-motion resonances] of the center of the family. Comparing the distribution of physical parameters of the family members to that of the local background will allow us to assess the likelihood that the family is contaminated by the inclusion of background objects. Specifically, in the case of the albedo, the background will mostly have a bimodal distribution, while families are expected to have a monomodal distribution consistent with formation from a single-parent body. Here, we regard the distribution of physical parameters which have been observed for a large number of objects: reflectance spectra, albedos, colours, and phase curve parameters. We further include taxonomic classifications as a comparison criterion.

For all members of the candidate families and local backgrounds, we retrieve available physical parameters from the literature using SsODNet (https://ssp.imcce.fr/webservices/ssodnet/, accessed on 2023 February 14), a web service from the Institut de mécanique céleste et de calcul des éphémérides (IMCCE), which contains a compilation of data from over 3000 peer-reviewed publications on minor bodies (Berthier et al. 2022b), including those published in the surveys of Bus & Binzel (2002), Lazzaro et al. (2004), and DeMeo et al. (2009); the Sloan Digital Sky Survey-Moving Object Catalog data (SDSS-MOC4; Ivezić et al. 2001) used with the taxonomical method of DeMeo & Carry (2013) and Sergeyev & Carry (2021); and albedo data in the WISE and NEOWISE, AKARI, or IRAS data bases (Ryan & Woodward 2010; Usui et al. 2011; Masiero et al. 2012), among other sources. All the relevant papers from which data and methodologies have been used in this work are listed in the appendix 9.

For albedo data, where an object had multiple albedo measurements in the *WISE* and NEOWISE data, we chose the one with the smallest listed diameter uncertainty, as this will be the strongest metric for the quality of the physical property fit used to derive albedo from infrared data. We further search for reflectance spectra in the *Gaia* DR3 data (Gaia Collaboration 2022) and in a compilation of $\simeq$7000 spectra created by Mahlke, Carry & Mattei (2022a) in their work on asteroid taxonomy. Taxonomical classification for reflectance spectra in *Gaia* DR3 can be obtained using classy (https://github.com/maxmahlke/classy/), a classification algorithm that can handle missing data and includes the visual albedo, when possible. Before classifying the *Gaia* spectra, we remove reflectance values that carry the photometric flags 1 and 2, indicating low quality. We further remove data points with a signal-to-noise ratio lower than 10. The systematic reddening towards the ultraviolet is corrected following Tinaut-Ruano et al. (2023).

Finally, Mahlke, Carry & Denneau (2021) showed that asteroids with different taxonomic classes display different behaviours in the (G_1, G_2) phase curve parameter space. When possible, we will discuss taxonomic information obtainable from this method for the groups studied in this work. As we aim to identify different statistical distributions between the candidate families and their background populations, we require a sufficiently large number of physical parameters for the families' members. This is, in particular, relevant for properties such as phase curve parameters, which exhibit large stochastic uncertainties when derived based on non-targeted observations for a large number of objects. Our general results will be discussed in the next subsections.

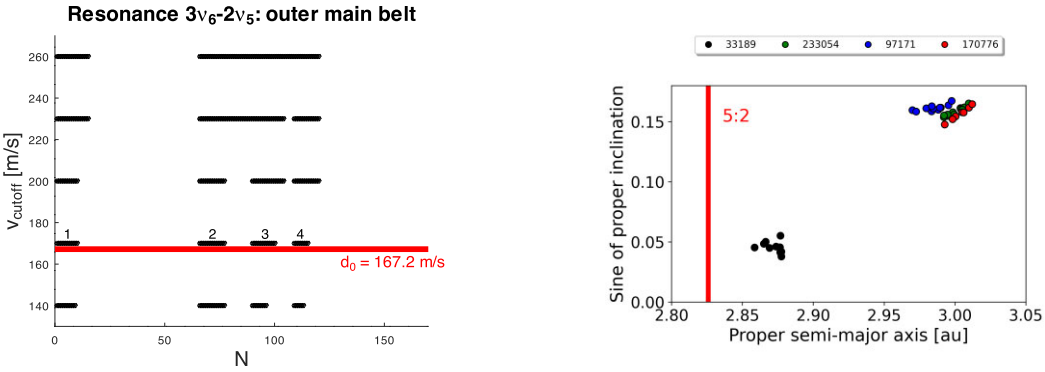

Figure 8. Left panel: A stalactite diagram for the asteroids in the $3\nu_6 - 2\nu_5$ resonance. The numbers on the plot identify the groups, according to the nomenclature of Table 4. Right panel: A proper (a, $\sin(i)$) distribution of the resonant asteroid groups identified in this work.

Table 4. Identification of the asteroid groups interacting with the $3\nu_6 - 2\nu_5$ secular resonance identified in this work. The fifth column displays the velocity cut-off for which the families join the Koronis (group 33189) and the Eos (remaining groups) asteroid families, and the last the number of multi-opposition asteroids identified as possible family members.

Group #	Asteroid id.	Asteroid name	# of members	Velocity cutoff (m s^{-1})	# multi-opp. asteroids
1	33 189	(1999 GV_3)	10	140	5
2	233 054	(2005 GA_{88})	12	80	4
3	92 171	(1999 VE_{195})	11	110	15
4	170 776	(2004 CA_{95})	7	50	0

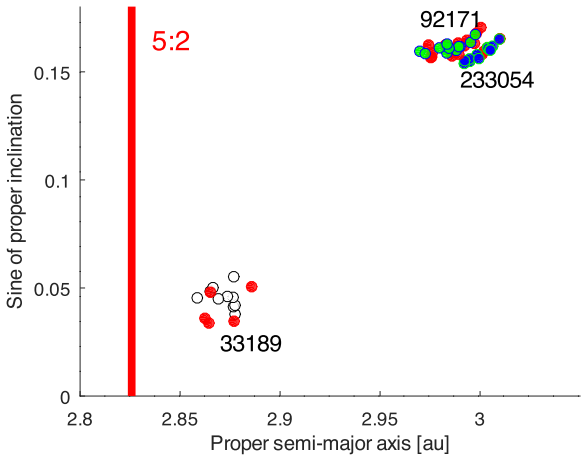

Figure 9. An (a, $\sin(i)$) projection of the numbered populations of the 59421, 233054, and 92 171 groups (symbols are the same as in Fig. 8). The filled red circles show the location of the extended population among multi-opposition asteroids for the three clusters.

5.1 $2\nu_6 - \nu_5$ resonance

Table 5 shows information for each group about taxonomy, spectra, colours, albedo, and phase curve parameters. The 2198 group is the one most closely associated with the Astraea family: almost 100 per cent of the 345 family members which have been associated with a family in the literature have been associated with the Astraea family (see Fig. 10, bottom right panel). Of the 30 per cent of family members with taxonomic classifications, the majority has been classified as S-type. The background shows a similar distribution. We exclude classes with fewer than 20 members from the histogram of the background population to increase the readability. 2198 is the only family where we have sufficient *Gaia* spectra to make a tentative ensemble classification. Out of 621 family members, 74 have a spectrum in *Gaia* DR3 (second row on the left in Fig. 10), and 67.0 per cent belong to S-complex taxonomies. Taxonomy classification based mostly on SDSS colours also shows a mixed distribution with a tendency towards the S-complex. Albedos, mostly computed from *WISE* data, have a bimodal distribution with 61.6 per cent of family members showing albedos above 10 per cent. Given that this includes M-complex members, the albedo distribution thus indicates a lower percentage of S-types than what observed from spectra, colours, and taxonomic classifications. However, the discrepancy might be fully explained by (i) different sampling constraints, with SDSS being more sensitive to small, S-complex objects and NEOWISE having a relatively flat selection effect concerning albedo (cf. Mainzer et al. 2012); and (ii) uncertainty of taxonomic classification based on visible-only photometry. Finally, most family members fall into the S-type regime of the G1–G2 phase curve parameters' space (see Fig. 10, bottom left panel).

The 5507 group has 1 CX asteroid (12664) and 1 S-type (57354) (see the left panel of Fig. 11). 12 664 and 19639 can both be albedo interlopers, as also shown in the right panel of Fig. 11. The albedo distribution for this family shows a significantly larger fraction of high-albedo objects than the background, implying that this is likely a high-albedo family with a small amount of background contamination. Results from phase curve parameters and taxonomy point to a mixed composition, but we are affected by small numbers statistics for this and the remaining groups in the $2\nu_6 - \nu_5$ resonance. Discussions of the physical properties of the remaining candidate families should be taken with a grain of salt.

The 6573 group is possibly an S-type complex with a possible C-type interloper, 6573 itself. 3 albedo interlopers are found in the S-complex 11 791 group. 41895 is a possible C-complex group, with

Table 5. Physical properties of the asteroid groups interacting with the $2\nu_6 - \nu_5$ secular resonance identified in this work. The fifth column displays the likely taxonomic complex from our analysis. The sixth column shows results from *Gaia* spectra. The sixth column reports data on colours, the seventh on albedo and the eighth the mean value of albedo for the family. Finally, the last column shows the taxonomy most compatible with the phase curve parameters distribution.

Group #	Asteroid id.	Asteroid Name	# of members	Taxonomy	Spectra	Colours	Albedo	Mean p_V	Phase curve parameters
1	2198	Ceplecha	621	S	S	S(64.8 per cent)	S(61.6 per cent)	0.183	S
2	5507	Niijima	14	Mixed	S	C(66.6 per cent)	S(75.0 per cent)	0.221	Mixed
3	6573	Magnitskij	16	S	–	S(56.3 per cent)	S(100.0 per cent)	0.144	–
4	11 791	Sofiyavarzar	40	S	–	S(71.0 per cent)	S(71.4 per cent)	0.239	–
5	41 895	(2000 WJ_{121})	13	–	–	C(50.0 per cent)	C(100.0 per cent)	0.070	–
6	17 200	(2000 AF_{47})	16	–	–	S(65.7 per cent)	S(66.7 per cent)	0.111	–
7	14 611	Elsaadawi	11	S	–	S(71.4 per cent)	S(100.0 per cent)	0.317	S
8	47 883	(2000 FZ_{39})	11	Mixed	–	C(50.0 per cent)	C(100.0 per cent)	0.053	–

possible S-type interlopers, like (97258). 17 200 and 14 611 have all taxonomies compatible with an S-complex composition, with one possible albedo interloper for 17200. Finally, 47 883 has three asteroids with S-complex taxonomies, and 5 objects with C-complex albedos, making its classification rather ambiguous.

Except for 41 895 and 47883, all the other groups appear to be compatible with an S-complex composition, with various percentages of interlopers.

5.2 $3\nu_6 - 2\nu_5$ resonance

None of the members of the asteroids' groups in the $3\nu_6 - 2\nu_5$ resonance has any member for which information in one of the spectroscopical surveys is available. Information on *Gaia* spectra or phase curve parameters is also unavailable for all the $3\nu_6 - 2\nu_5$ candidate families. Table 6 shows colour and albedo information for the studied groups.

For the 33 189 group, three objects have colour information. 33189 Ritzdorf Sq spectral type could be compatible with an origin from the Koronis family and supports the possibility of this family being part of the extended Koronis group. No albedo information is available for any of the family members. The local background is dominated by low-albedo objects.

Limited information is available for the 233 054, 92171, and 170 776 groups, with up to 5 asteroids with known albedos, all with $p_V < 0.12$. The physical properties of the 170 776 group and of surrounding main belt asteroids are shown in Fig. 12. As the outer belt is dominated by low albedo objects, the current data are insufficient to quantify the level of any background contamination.

6 DATING THE NEW RESONANT FAMILIES

Asteroid families can be dated using various approaches. One of the most commonly used is based on using the slope of the V-shape of family members in the (a, $1/D$) domain (Spoto, Milani & Knežević 2015). Other methods use Monte Carlo simulations of the Yarko-Yorp dynamical diffusion of family members Vokrouhlický et al. (2006a). Both such approaches require a sample of asteroids of at least 100 members to work properly (Vokrouhlický et al. 2006a; Spoto, Milani & Knežević 2015). For smaller, younger clusters methods based on time-reversal numerical simulations, like the Backward Integration Method (BIM; Nesvorný et al. 2002) and the Close Encounters Method (CEM; Pravec et al. 2010), can provide accurate and precise age estimates.

In the BIM technique, previous differences in the longitudes of the pericenter ϖ and node Ω of family members with regard to those of the claimed parent body are determined through time-reversal numerical simulations. During the period of family formation, these discrepancies should settle to levels that are close to zero. The approach can only employ convergence in Ω for asteroids inside g-type secular resonance, when ϖ is in a locked state, but the main idea is the same. According to Radović (2017), BIM can detect families with ages up to 18 Myr, so in this work we integrated our groups backward in time for timescales of 20 Myr.

The CEM strategy functions by simulating many clones of the parent body and the other family members in the past. The Hill's radius and the main body's escape velocity are used to set the cutoff values for the relative distances and speeds of the encounters. Close interactions between two clones that take place at low relative speeds and distances are observed. The median value of these periods is used to calculate the pair's age, while the confidence interval covers the periods between the 25th and 75th quantiles of the distribution. The techniques section of Carruba et al. (2020) has further information on both of these methods as applied by our team. CEM can detect young asteroid families with ages up to $\simeq 7$ Myr. Our numerical simulations will cover timescales of 10 Myr into the past.

Finally, as detailed in Carruba et al. (2020), fission pairs may form inside relatively young asteroid families. We define fission pair candidates as pairs of asteroids with relative distances in proper elements, determined using equation (4) in Carruba et al. (2020), of less than 5 m s^{-1}, and a mass ratio (see equation 5 in Carruba et al. 2020) of less than 0.3. We searched for candidate pairs in all families identified in this work, and the results will be discussed in the next sections.

6.1 $2\nu_6 - \nu_5$ resonance

We searched for possible young asteroid groups using BIM for the clusters identified in the $2\nu_6 - \nu_5$ resonance. Of the eight identified clusters, only the 5507 Niijima group had a possible age of less than 20 Myr. Our results are shown in Fig. 13, where we observe two possible convergences of the angles at 2.5 ± 1.3 Myr and 5.5 ± 0.8 Myr[1]. Since we are neglecting Yarkovsky forces,

[1]At this stage of our study, we do not include in our simulations the effect of the Yarkovsky force, since proper modeling of this effect would require creating a population of several hundreds of clones of each asteroid simulating the generally unknown parameters of the Yarkovsky effect, like the object density, surface density, thermal conductivity, spin obliquity, etc. We believe that such a detailed study exceeds the goal of this paper, which is to perform a preliminary exploration of young asteroid families in secular resonance configurations.

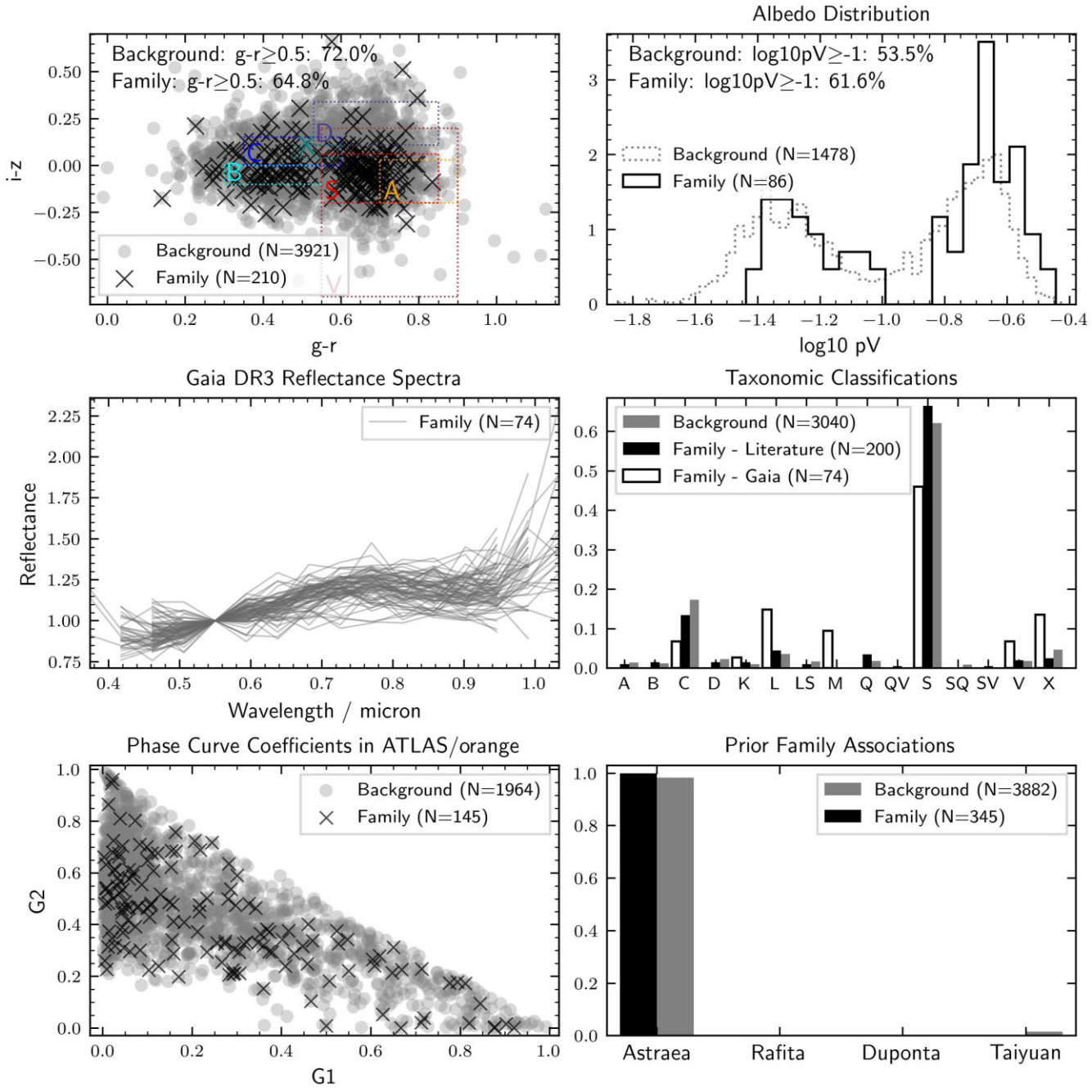

Figure 10. Physical properties of the 2198 candidate family. We display the $(g - r, i - z)$ colours of the family (black crosses) and local background object (grey circles), with the class boundaries from Sergeyev & Carry (2021) (top left panel), the albedo distribution of family and background objects (top right panel), the *Gaia* DR3 spectra (middle left panel), the known taxonomical properties of family and background objects (middle right panel), the projection of family and background members in the (G_1, G_2) plane (bottom left panel), and the fraction of members belonging to known asteroid families (bottom right panel).

and it is not possible to obtain convergence in ϖ, these are just qualitative estimates of the real age. To obtain a confirmation of the age estimate, we applied CEM to all the asteroid pairs present in this group. At this stage of our investigation, we also include possible taxonomical interlopers like 12664, which is a CX interloper in an S group, and 19639, which is a likely albedo interloper. Should these objects not be a part of the family, we will expect them to have CEM ages significantly different from the rest of the group, which may constitute independent proof of the validity of the CEM approach. The right panel of Fig. 13 shows our results for the pair 5507–125592, which has an estimated nominal age of $5.32^{+1.57}_{-2.95}$ Myr. Table 7 displays our results for all the other asteroid pairs in the family. All age estimates are statistically significant, having been obtained from several thousands of possible encounters at low relative speeds and distances. Using the approach of Carruba et al. (2022b) for determining age estimates from CEM, with their errors (see equations 2 and 3 in the cited reference), we found an age for the 5507 Niijima family of 5.25 ± 1.88 Myr.

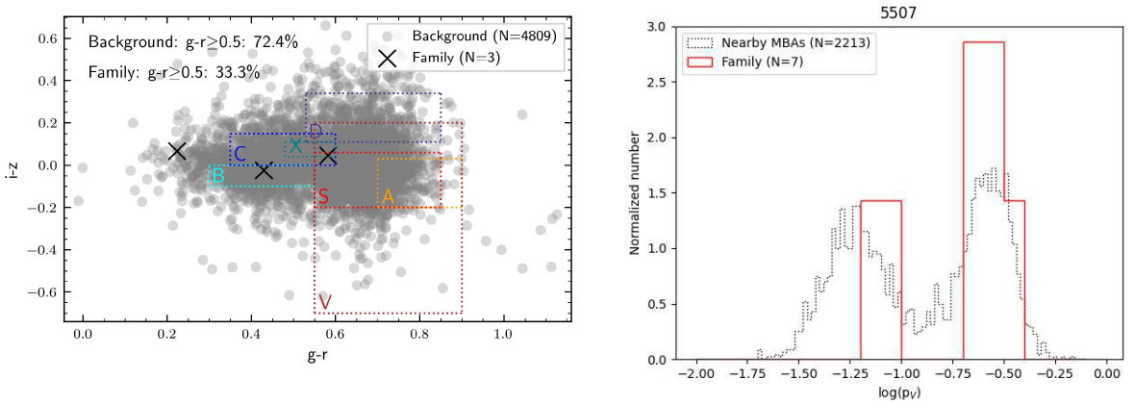

Figure 11. Physical properties of the 5507 candidate family. On the left panel, we display the $(g - r, i - z)$ colours of the family (black crosses) and local background object (gray circles), while the right panel shows the albedo distribution of family (red line) and background objects (dashed black line).

Table 6. Physical properties of the asteroid groups interacting with the $3\nu_6 - 2\nu_5$ secular resonance identified in this work. We present data on colours (fifth column), albedo (sixth column), and the mean value of visual albedo (seventh column) for the studied groups.

Group #	Asteroid id.	Asteroid Name	# of members	Colours	Albedo	Mean p_V
1	33 189	Ritzdorf	15	3 (S?)	0 -	-
2	233 054	(2005 GA_{88})	16	3 (C?)	3 (C?)	0.055
3	92 171	(1999 VE_{195})	26	4 (C?)	5 (C?)	0.033
4	170 776	(2004 CA_{95})	7	1 (C?)	3 (C?)	0.058

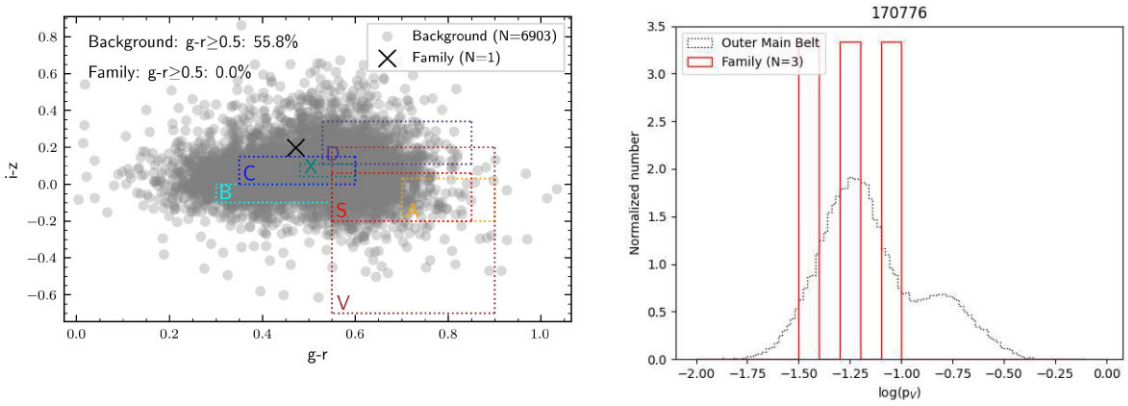

Figure 12. Physical properties of the 170 776 candidate family. We use the same scheme employed for Fig. 11.

The age obtained from CEM appears to be older than the first result from BIM, but compatible with the second one. Two pairs, the ones with 12 664 and 19639, appear to have ages older than the rest of the family. To check for the possible existence of sub-groups inside the 5507 cluster, we apply a DBSCAN clustering algorithm (Ester et al. 1996) to data in the plane age versus absolute magnitude, with a procedure similar to that proposed in Carruba et al. (2020).

DBSCAN is a density-based clustering algorithm that groups together points that are close to each other in a high-density region of the data space. The radius of the area surrounding each data point is designated as 'eps.' It establishes the minimum separation required between any two points in order to classify them as belonging to the same cluster. The bare minimum of points needed to create a dense zone is called 'min_samples'. This parameter determines the minimum size of a cluster. Here, we uses eps = 0.5 and min_samples=5, which are the default value.

We identified three possible groups, one of smaller objects with high absolute magnitudes, an intermediate one with objects with $15 < H < 16$, and the group formed by the two pairs with 12 664 and 19639, with higher ages (see Fig. 14). The ages from the high and intermediate absolute magnitude groups are comparable. If we exclude the two older pairs, associated with likely interlopers, the estimated family age drops to 4.90 ± 1.60 Myr, which is compatible with the second possible age interval from BIM. We did not detect possible fission pairs in the Niijima group or any of the other possible families.

6.2 $3\nu_6 - 2\nu_5$ resonance

Among the four studied groups, only the 170 776 cluster showed a possible young age with BIM, with two preliminary ages of 1.4 ± 0.4 and 4.7 ± 0.7 Myr. The family extends beyond librating objects

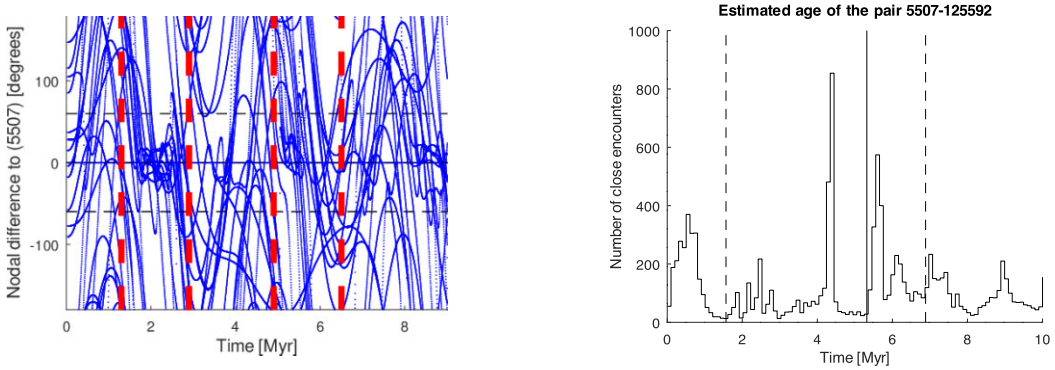

Figure 13. Left panel: Convergence of nodal distances to the parent body of the 5507 Niijima group as a function of time. The vertical dashed lines display the uncertainty levels for the two possible age solutions. Right panel: Distribution of close encounter times for the pair 5507–125592. The vertical line displays the age estimate from CEM, while the dashed lines show the uncertainty levels.

Table 7. Age estimates for pairs in the 5507 Niijima cluster obtained with CEM.

Asteroid Id.	Number of enc.	Age (Myr)
12 664	22 129	$6.13^{+1.45}_{-2.83}$
19105	6090	$5.14^{+2.63}_{-2.41}$
19639	13 923	$7.16^{+1.96}_{-3.00}$
24274	14 906	$5.65^{+1.39}_{-1.76}$
38755	6185	$4.63^{+2.53}_{-3.80}$
57354	5996	$5.06^{+2.07}_{-4.08}$
63562	11 293	$5.36^{+1.52}_{-3.00}$
116120	12 915	$4.73^{+2.20}_{-1.29}$
125592	11 406	$5.32^{+1.57}_{-2.94}$
222567	10 896	$4.43^{+2.31}_{-2.57}$
255962	14 890	$3.91^{+3.02}_{-3.06}$
302951	12 056	$5.15^{+1.93}_{-2.09}$
380822	5543	$5.21^{+1.96}_{-2.78}$

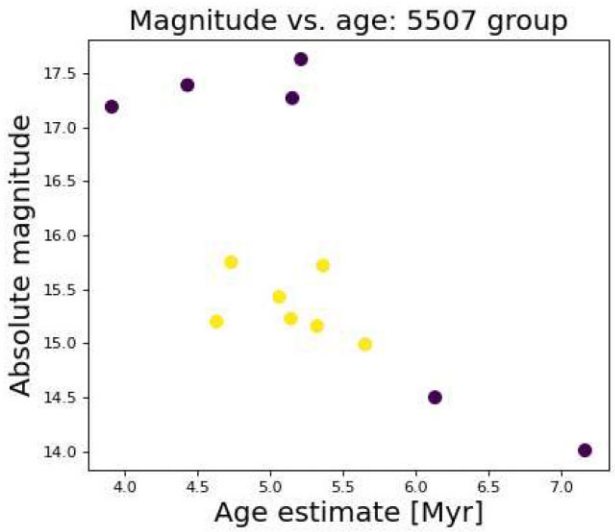

Figure 14. An absolute magnitude versus age diagram for the members of the 5507 Niijima group. The colour code is associated with the three groups identified by the DBSCAN machine learning algorithm.

when standard HCM is used on asteroid proper elements and merges with the Eos family at a cut-off of 50 m s^{-1}. The largest group before the merging has 21 members. We checked with BIM possible convergences of the Ω angles of these asteroids in the past, and we identify 13 objects that show the same solutions observed for the already known resonant members. The left panel of Fig. 15 shows the time dependence of the convergence of nodal distances for these 13 objects. Of the 7 new possible members, 53 790 (2000 EV_{105}) has a rather larger albedo than the rest of the group. Its p_V is 0.29, while the average value for the group is 0.055 ± 0.015. This object may be an interloper. Since at this stage of our analysis, it is not clear which asteroid may be the parent body, we decide to use 170776 as such for CEM. The right panel of Fig. 15 displays the age estimate from CEM for the pair 170776–469020, while Table 8 shows our results for all the pairs in the family. Again, age estimates are statistically robust, having being determined upon several thousands of close encounters. Using the same approach of Section 6.1, we found an age of 6.13 ± 2.76 Myr.

As observed for the resonant family in the $2\nu_6 - \nu_5$ resonance, this age estimate is older than what is expected from BIM. Again, there are pairs whose ages are significantly older than the rest of the family. Fig. 16 displays our DBSCAN results for the new resonant family. The pairs with 53 790 and 491 469 have larger age estimates that are incompatible with the age obtained from CEM for the rest of the family. Both objects may be interlopers, which is confirmed by the rather divergent value of albedo of 53 790. Eliminating these two objects yields a lower age estimate of the family, with an estimated age of 5.10 ± 1.51 Myr. No possible fission pairs were detected among the $3\nu_6 - 2\nu_5$ resonance groups.

7 RESONANT PROPER ELEMENTS AND CONSTRAINTS ON THE INITIAL EJECTION VELOCITY FIELD OF *g*-TYPE RESONANT FAMILIES

It is well known that the non-linear secular resonances, including the ones we are dealing with in the present study, give rise to the comparatively large and fairly regular oscillations of asteroid orbital elements, which cannot be averaged out if the object is in libration. The problem was circumvented in the analytical proper elements computation (Milani & Knežević 1992) by simply leaving the resonant oscillation unremoved, at the price that the proper elements of such bodies suffered from severely deteriorated accuracy, sometimes even to the point that they became unusable for the family

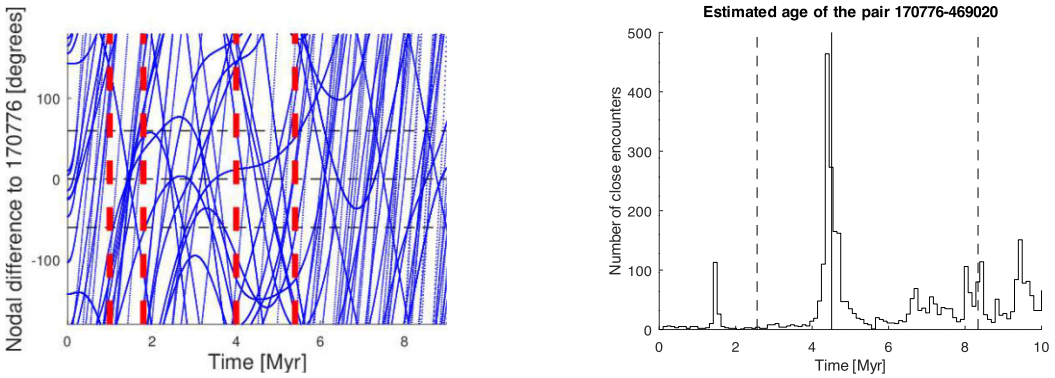

Figure 15. Left panel: Convergence of nodal distances to the parent body of the 170 776 (2004 CA_{95}) group as a function of time. Symbols are the same as in Fig. 13. Right panel: Distribution of close encounter times for the pair 170 776–469 020. The vertical line displays the age estimate from CEM, while the dashed lines show the uncertainty levels.

Table 8. Age estimates for pairs in the 170 776 (2004 CA_{95}) cluster obtained with CEM.

Asteroid Id.	Number of enc.	Age (Myr)
53 790	3754	$7.10^{+1.46}_{-2.06}$
92217	2389	$5.66^{+1.75}_{-2.73}$
133913	2651	$4.39^{+2.99}_{-2.32}$
216691	3916	$5.39^{+1.86}_{-0.30}$
250792	3281	$5.38^{+2.32}_{-0.84}$
399185	2053	$5.18^{+2.19}_{-1.36}$
418738	1926	$4.51^{+3.15}_{-3.22}$
469020	3585	$5.78^{+2.56}_{-1.40}$
487095	2020	$4.15^{+3.75}_{-1.12}$
491469	3787	$7.54^{+1.13}_{-3.26}$
541352	2424	$4.33^{+3.12}_{-0.39}$
610139	2389	$4.79^{+2.53}_{-0.54}$

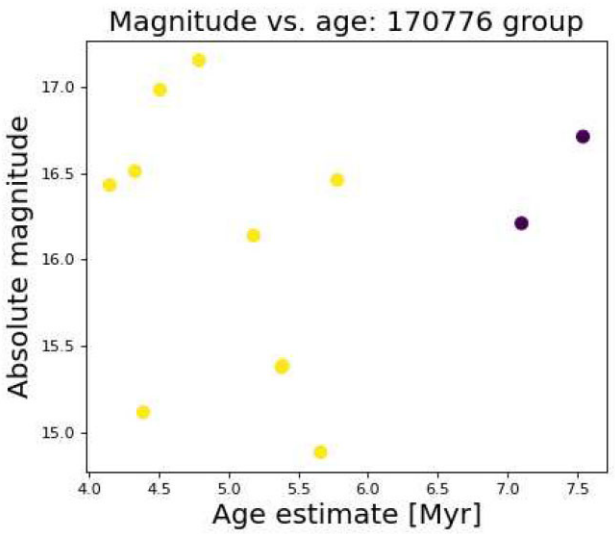

Figure 16. An absolute magnitude versus age diagram for the members of the 170 776 (2004 CA_{95}) group. The colour code is associated with the two groups identified by the DBSCAN machine learning algorithm.

classification purpose; in such a case the appropriate 'resonant flag' has been attached to the data as a warning for the user.

The first attempt to attack the problem by computing specially adapted 'resonant proper elements' is due to Morbidelli (1993), who computed the secular evolution using the Hamiltonian which resembles an integrable single resonance normal form, determining the so-called *s*emiproper action-angle variables, and converting them to the proper eccentricity and inclination corresponding to a specific value of the argument of perihelion ($g = 0$).

In this paper, we also use a kind of resonant proper elements, but computed by means of a simpler numerical method proposed by Milani et al. (2017), specifically adapted for a given secular resonance. In the 'g-type' resonances case, the only element which is seriously affected by the resonant perturbation is the eccentricity e, thus new resonant value has to be defined just for this element. Milani et al. (2017) adopted the amplitude Δe of libration in eccentricity, associated with the libration of the critical argument, to serve as the new proper element, since this amplitude exhibits the property of remaining nearly constant in time, in any case much more so than the eccentricity itself. A purely numerical procedure is used to compute this amplitude of libration, starting from the output of numerical integration filtered online to remove short-periodic perturbations (for a standard 10 Myr integration time span, we removed oscillations with periods $\lesssim$750 yr). The time-step of numerical integrations is selected automatically by produce an optimal truncation error in longitude according to the procedure described in (Milani & Nobili 1988), and it does not exceed 0.2 d. The time series of filtered non-singular variables are next smoothed (filtered again) with decimation 100 to remove oscillations with periods up to 75 000 yr. Note that this removal is justified because typical libration periods for resonant asteroids may be significantly longer (over 1 Myr).

For the resulting doubly filtered eccentricity time series, we next compute spectrum for periods in the range of values depending on the resonance (see below), then we determine the maximum spectral density following Ferraz-Mello (1981) and adopt the corresponding amplitude as the proper element. The stability in time is estimated by means of the running box method, with errors obtained as RMS of the series of consecutive values of amplitudes computed over shorter intervals of time. The integration length is adjusted so as to always have at least 20 000 records in the time series.

We computed resonant proper elements for members of the two families of interest, the 5507 in the $2\nu_6 - \nu_5$ and the 170 776 in the $3\nu_6 - 2\nu_5$. Dealing with two resonances of different orders, we had to optimize the procedure for each of them separately. For this purpose,

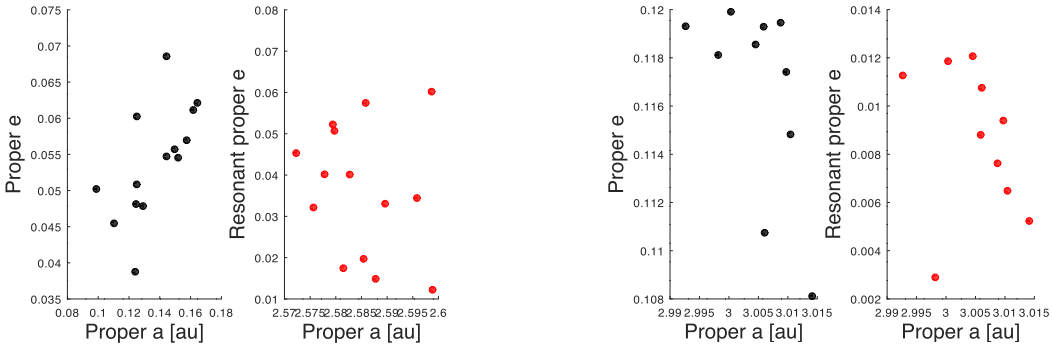

Figure 17. In the left panel, we show the standard synthetic (black full circles) and resonant proper (red full circles) (a, e) distribution for the 5507 asteroid family. The right panel shows the same for the members of the 170 776 family for which resonant proper elements can be computed.

we first made a shorter integration (10 Myr) to assess the likely libration periods of resonant asteroids and to adjust the integration time-span and the range in which to compute the spectrum, to achieve the highest accuracy of the results.

Adopting the aforementioned criterion ± 0.2 arcsec yr^{-1} as a distance from the exact resonance within which according to Carruba (2009) asteroids are likely to be in libration, we were able to compute the resonant proper elements for all the asteroids in the 5507 group. Since libration periods for these objects turned out to be in the range 2.8−3.8 Myr, we decided to integrate the whole set for 30 Myr, to have 9 shorter intervals of the length of 6 Myr, shifted by 3 Myr. This enabled a reliable stability estimate and accurate derivation of the amplitude Δe from the spectrum computed for periods between 1 and 6 Myr. Indeed, the results we have obtained showed that errors are typically an order of magnitude smaller than the corresponding amplitudes, except in two cases (asteroids 19 639 and 302 951) for which the errors are somewhat larger, but still significantly less than the amplitudes themselves.

For the 170 776 group, the resonant proper elements could only be computed for the following 10 asteroids: 53 790, 92 217, 133 913, 399 185, 418 738, 469 020, 487 095, 491 469, 541 352, and 610 139. The others are more distant from a resonant configuration, and our procedure was not applied for these objects. Still, the results were good enough for the subsequent analysis. In this case, the libration periods ranged from 7 to 13 Myr, hence we extended the integration time span to 100 Myr, computing spectrum for 6−15 Myr range. The accuracy of the obtained resonant proper elements was very good, with a couple of cases (asteroids 133 913 and 399 185) that had somewhat larger errors due to more complex dynamics (a very long term effect of unidentified origin, giving rise to irregular eccentricity oscillations, in the former case, and exit from the resonance, interrupting the libration after some 70 Myr, in the latter). The results of our computations are shown in Fig. 17.

For g-type secular resonance, we expect that at the simplest level of perturbation theory the quantity:

$$K_2^{'} = \sqrt{1-e^2}[1-\cos(i)], \tag{1}$$

should be preserved, when resonant proper eccentricity is used, rather than the unstable standard proper e. In the next subsections, we will investigate the preservation of this conserved quantity for the two studied families. Under the assumption that this is true, an approach not often available for non-resonant families can be used to estimate the initial ejection velocity field thanks to the retention of the original values of $K_2^{'}$ (Vokrouhlický et al. 2006b, see also the review in Carruba, Vokrouhlický & Novaković 2018).

To proceed, let's first suppose that asteroids are ejected with an isotropic ejection velocity field and that the standard deviations $V_{\rm SD}$ are proportional to the size of the asteroid through the parameter $V_{\rm EJ}$, as shown by the relationship:

$$V_{\rm SD} = V_{\rm EJ} \cdot \left(\frac{5\ {\rm km}}{D}\right), \tag{2}$$

where D is the asteroid's diameter in kilometers. The ejection velocities for asymmetric fields may not be precisely measured by this method, but it can place helpful limits on their magnitude. We simulate several asteroid families using different $V_{\rm EJ}$ parameter values, calculate their $K_2^{'}$ numbers, and then choose the one that best matches the observed $K_2^{'}$ distribution.

To test this numerically, we may use a variable that is similar to a χ^2 variable and is specified as equation (3):

$$\chi^2 = \sum_{i=1}^{N_{int}} \frac{(q_i - p_i)^2}{q_i}. \tag{3}$$

The number of intervals required to produce the histogram of the $K_2^{'}$ distribution is $N_{\rm int} = 6$. The number of actual and virtual objects in the ith interval are represented by q_i and p_i, respectively.

After values of $\Delta\chi^2 = \chi^2 - {\chi^2}_{\rm min}$, where ${\chi^2}_{\rm min}$ is the smallest value of χ^2, are acquired, the χ^2 probability distribution function can be used to calculate the 97.5 per cent confidence level (for a further explanation of this procedure, see Carruba, Vokrouhlický & Novaković 2018). Applications of this procedure will be discussed in the next subsections.

7.1 $2\nu_6 - \nu_5$ resonance

First, we verified that the distribution of $K_2^{'}$ values is preserved when using resonant proper e. The left panel of Fig. 18 shows the initial and final distributions for the first and last time interval used to compute resonant proper e. Applications of Kolmogorov–Smirnov tests to compute the probability that the initial and any of the successive $K_2^{'}$ distributions are compatible all passed with p-values larger than 0.90, which suggest that the $K_2^{'}$ distribution was rather stable over the studied time-interval.

Then we estimated the $V_{\rm EJ}$ parameter with the approach used in Section 7. Our results are shown in the right panel of Fig. 18. For the 5507 group, we found $V_{\rm EJ}$ to be 10^{+11}_{-1} m s^{-1}.

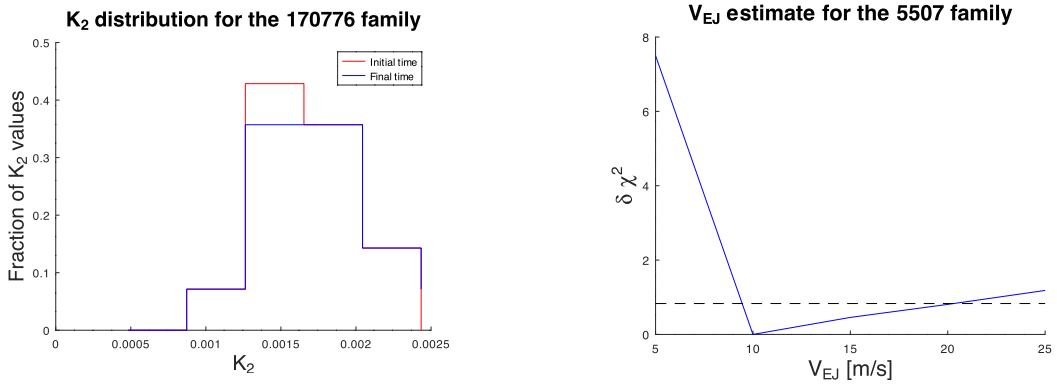

Figure 18. In the left panel, we show the distributions of $K_2^{'}$ values for the initial (red line) and final (blue line) time interval used for computing resonant proper elements for the 5507 group. The right panel displays the dependence of $\Delta\chi^2$ as a function of the $V_{\rm EJ}$ parameter. The 97.5 per cent confidence level limit is identified by the horizontal dashed line.

7.2 $3\nu_6 - 2\nu_5$ resonance

We again applied the procedure described in Section 7.1 and verified the conservation of the $K_2^{'}$ quantity distribution. Kolmogorov–Smirnov tests confirms the stability of the $K_2^{'}$ quantity distribution with p-values larger than 0.98. Results are shown in the left panel of Fig. 19.

Then, we used the method described in Section 7 to estimate the $V_{\rm EJ}$ parameter. Our results are shown in the right panel of Fig. 19. For the 170 776 group, we estimate $V_{\rm EJ}$ to be 20^{+1}_{-4} m s^{-1}.

8 ESTIMATING THE PROBABILITY OF PRODUCING YOUNG RESONANT ASTEROID FAMILIES

The cumulative number of impacts, $n(t, d)$, of asteroids larger than d in the last t years, on any target, can be represented as:

$$n(t, d) = F(< t)\, N(> d), \tag{4}$$

where $N(> d)$ is the number of asteroids larger than d (the size frequency distribution – SFD), and $F(< t)$ is the cumulative probability of impacts on the specific target in the last t years (the chronology function). The slope of $F(< t)$ is related to the so-called intrinsic collision probability, which is the probability per unit of cross-section:

$$P_i(t) = \frac{4\pi}{S}\frac{{\rm d}F}{{\rm d}t}, \tag{5}$$

where $S = \pi D^2$ is the surface area of the target, and the factor 4π accounts for the difference between surface and cross-section (Wetherill 1967). With this definition, the number of impacts, dn, from impactors larger than d, on a target of size D, over an interval dt, is given by

$${\rm d}n(t, d) = \frac{1}{4} P_i(t) D^2 N(> d){\rm d}t. \tag{6}$$

In the above calculation, it is assumed that the SFD does not change with time, which is a good assumption over the last 3.9 Gyr (Bottke et al. 2005). But there is the problem of the completeness limit, which is different for different parts of the MB. Since we are dealing with small parent bodies, the SFD must be extrapolated beyond the completeness and this is a huge source of uncertainty. Here, we will assume a unique SFD for all the MB, with an extrapolation rule (Roig & Nesvorný 2020):

$$N(> d) = 10^{6.5} d^{-2.6}, \qquad d < 8.7 \text{ km}.$$

As for the intrinsic collision probability, it has also been constant over the last 3.9 Gyr. Early estimates give a value of 2.85×10^{-18} km^{-2} yr^{-1} for the whole MB (Farinella & Davis 1992), but again P_i has different values for different parts of the MB (actually, the P_i has specific values for each individual asteroid because it depends on a, e, i). Moreover, for a given region of the MB, there are several values of P_i, depending if you consider intra-region collisions of inter-regions collisions (Cibulková, Brož & Benavidez 2014). Intra-region probabilities are always the largest. Here, we will always consider the maximum P_i in the corresponding region of the MB in order to maximize the impact probability.

Under the above assumptions, $n(t, d)$ increases linearly with time, and the mean time required to have at least one impact, $n = 1$, is then

$$\tau = \frac{4}{P_i D^2 N(> d)}. \tag{7}$$

The actual probability of having 1 impact over τ follows a Poisson distribution. We are interested in collisions that are able to shatter the target in order to have the possibility of forming a family. During an impact, the result is determined by the specific impact energy, given by

$$Q = \frac{1}{2}\frac{d^3}{D^3 + d^3} v^2, \tag{8}$$

where v is the relative impact velocity and it is assumed, for simplicity, that both the target and the impactor have the same density, ρ. The average impact velocity among asteroids, $\bar{v}$, is of the order of 5 km s^{-1} (Farinella & Davis 1992) and has also been constant over the last 3.9 Gyr (Roig & Nesvorný 2020). But again, the values are slightly different in different regions of the MB. Here, we will always consider the largest possible value of $\bar{v}$ in the given region (Cibulková, Brož & Benavidez 2014), which maximizes the occurrence of catastrophic impacts.

The result will be catastrophic if $Q > Q_D^*$, where Q_D^* is the catastrophic threshold energy, necessary to disperse at least half of the mass of the target. This is given by a scaling law, and here in particular, we adopt the parametrization for monolithic basalt of Benz & Asphaug (1999):

$$Q_D^* = \frac{1}{q}\left[Q_0 \left(\frac{R}{1{\rm cm}}\right)^{-0.36} + B\,\rho \left(\frac{R}{1{\rm cm}}\right)^{1.36}\right], \tag{9}$$

where $Q_0 = 9 \times 10^3$ J kg^{-1} and $B = 5 \times 10^{-8}$ J m^3 kg^{-2}. The parameter $1 \leq q \leq 13$ has been introduced here ad hoc in order to

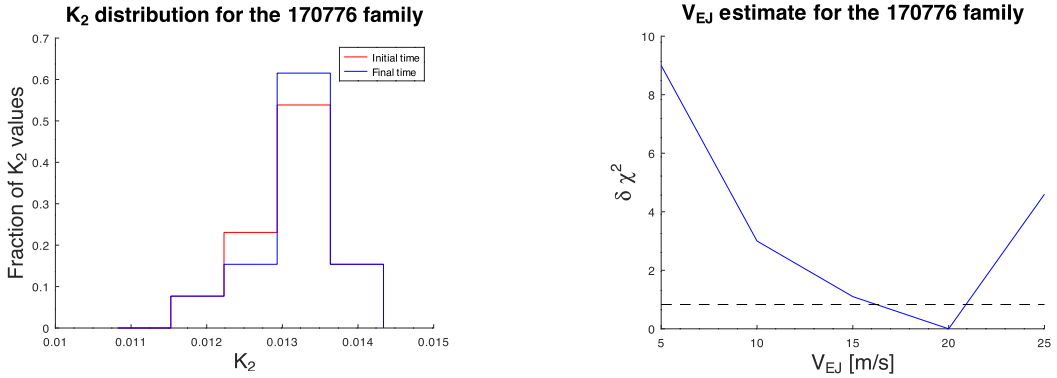

Figure 19. The same as in Fig. 18, but for the 170 776 group.

damp the threshold for rubble-pile asteroids, which should be easier to shatter than monolithic bodies ($q = 1$ is the original Benz and Asphaug law, larger values are for rubble-piles).

Although there are other parametrizations and other possible values of the parameters, the scaling laws have all the same behaviour: the stress. The largest uncertainties occur in the region of the transition from the stress to the gravity domains, $D_s < D < D_g$, which is around the size interval of the small families' parent bodies. We have now all the ingredients to make a rough estimation of the number of small families that you might expect to find in a given region of the MB:

(i) Start with the estimated diameter of the parent body D, the estimated age of the family T, and the intrinsic collision probability of the corresponding MB region P_i. For the age, we will consider the upper limit, $T_{\max}$.

(ii) Assume a density ρ for the parent body and determine the catastrophic threshold Q_D^* from equation (9).

(iii) Given $\bar{v}$ for the corresponding MB region, determine the minimum size of the impactors that are able to shatter the target from equation (8):

$$d_{\min} = \left(\frac{Q_D^*}{0.5\bar{v}^2 - Q_D^*} \right)^{1/3} D. \tag{10}$$

(iv) From the SFD, get the number $N(> d_{\min})$, and determine the rate of impacts from equation (6)

$$p_i = \frac{1}{4} P_i D^2 N(> d_{\min}).$$

(v) The expected number of catastrophic impacts that the target may have suffered over the age of the family is drawn from a Poisson distribution with mean

$$\bar{n}(T) = p_i T.$$

(vi) The above calculations correspond to a single body of size D. If you have $\mathcal{N}_{\rm PB}$ parent bodies of that size, the total amount of catastrophic collisions that you may expect during the last T is obtained by multiplying by $\mathcal{N}_{\rm PB}$. This should give the mean number of families that can be created in the last T

$$f_T = p_i T \mathcal{N}_{\rm PB}.$$

(vii) To compute $\mathcal{N}_{\rm PB}$, I considered an interval of $D \pm 0.05$ km from the SFD

$$\mathcal{N}_{\rm PB} = N(> D - 0.05) - N(> D + 0.05).$$

(viii) Finally, the actual number of expected families should be drawn from a Poisson distribution with mean f_T.

For the families that we are considering, results are in Table 9. Some caveats apply to these computations. Results are quite sensitive to the parameters used, especially the extrapolation of the SFD, the scaling law, and the assumed number of parent bodies. A more rigorous calculation should consider the SFD and $\mathcal{N}_{\rm PB}$ of each part of the MB separately. In this case, for a given region one would determine individual values of $\bar{n}(t)$, corresponding to the intra-region collisions and to the inter-regions collisions. The final $\bar{n}$ would be the sum of these. Finally, the above results are upper limits for almost monolithic bodies ($q = 2$), because we chose $P_i, \bar{v}, T$ in order to maximize the effects. But if we choose $q = 10$, for example, those upper limits of $f_{T_{\max}}$ increase by a factor of 4.

With these considerations, our results indicate that the formation of a young family like Zelima is extremely improbable. A ∼50 km body may suffer 0.1 collisions over 3.5 Gy, and since there are three of such bodies, you may expect ∼0.3 Zelima-like families formed over 3.5 Gyr, i.e. no family at all. The fact of having one of such families formed very recently is extremely rare and unique. The occurrence of families formed with smaller parent bodies, like those of 5507 Nijima and 170 776 (2004 CA_{95}) studied in this work, appear to be much more common occurrences, with values of $f_{T_{\max}}$ of 2.62 and 6.03, respectively. We believe that the use of methods for families determinations employed in this work, and the expected discovery of large numbers of new asteroids from surveys like the LSST, will significantly increase the number of known young families in secular resonance configurations, which will improve our knowledge about mechanisms of asteroid families formation.

9 CONCLUSIONS

The main goal of this paper was to obtain machine learning and deep learning models for resonant asteroids in the most diffusive g −type secular resonances. For this purpose, we obtained images and resonant statuses for more than 20 000 asteroids likely to interact with the $2\nu_6 - \nu_5$ and $3\nu_6 - 2\nu_5$ secular resonances. This allowed to identify 1694 $2\nu_6 - \nu_5$ and 210 $3\nu_6 - 2\nu_5$ resonant asteroids. For the case of the $2\nu_6 - \nu_5$ resonance, a deep learning CNN model was obtained and optimized to correct for possible overfitting issues (Carruba et al. 2022a), which will allow the classifications of future populations of resonant asteroids in time-scales of seconds.

Using the detected population of $2\nu_6 - \nu_5$ and $3\nu_6 - 2\nu_5$ resonators, we used standard HCM methods to identify 12 new possible dynamical groups among these librating populations. Most of these groups are not collisional families, but sub-groups of existing families, like Astraea, identified by HCM among the resonant

Table 9. Results of the collision probability model for the four young and resonant families.

	Tiffanykapler	Nijima	Zelima	(2004 CA_{95})
D (km)	10.4	9.0	55.4	7.0
T_{max} (Myr)	4.2	6.5	4.0	6.6
P_i (km^{-2}yr^{-1})	11.98×10^{-18}	4.91×10^{-18}	3.57×10^{-18}	3.57×10^{-18}
$\bar{v}$ (km s^{-1})	4.34	5.18	4.34	4.34
ρ (g cm^{-3})	2.5	2.5	2.5	2.5
q	2	2	2	2
d_{min} (km)	0.765	0.522	8.68	0.432
$N(> d_{min})$	6.34×10^{6}	1.484×10^{7}	11 464	2.805×10^{7}
τ (Myr)	487.0	677.8	31845.3	815.0
p_i (Myr^{-1})	2.053×10^{-3}	1.475×10^{-3}	3.14×10^{-5}	1.23×10^{-3}
$\bar{n}$(3.5Gy)	7.18	5.16	0.11	4.29
$\bar{n}(T_{max})$	8.62×10^{-3}	9.59×10^{-3}	1.25×10^{-4}	8.09×10^{-3}
$\mathcal{N}_{PB}$	181	273	3	745
$f_{T_{max}}$	1.56	2.62	3.77×10^{-4}	6.03

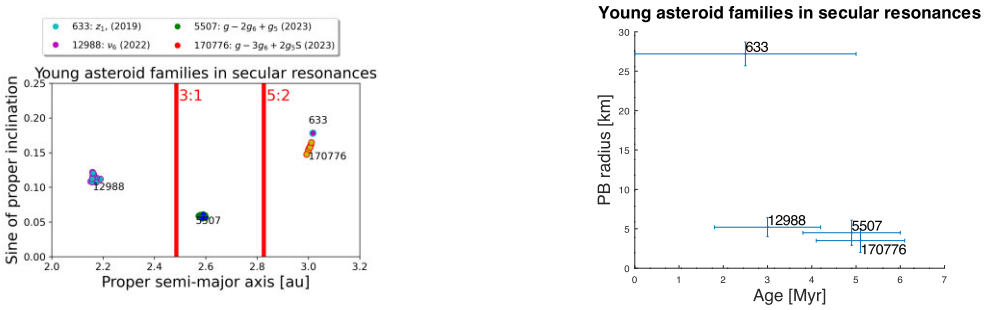

Figure 20. Asteroid families in secular resonances. Left panel: The $(a, \sin(i))$ distribution of the four currently known young asteroid families interacting with secular resonances. Right panel: The estimated parent body radiuses as a function of the age estimates, with their errors.

population. Multi-opposition asteroids were added to the core of the numbered objects using machine learning methods optimized through the use of genetic algorithms (Carruba et al. 2022b). The physical properties of the newly identified groups, like albedos and taxonomies, were then revised using currently available data bases.

Time-reversal numerical methods, like the BIM (Nesvorný et al. (2002) and the CEM (Pravec et al. 2010), were then applied to the newly identified groups to find possible young asteroid families, i.e. families with ages of 7 Myr or less. We identified the 5507 Niijima family in the $2\nu_6 - \nu_5$ resonance, and the 170 776 (2004 CA_{95}) family in the $3\nu_6 - 2\nu_5$, which are the first young asteroid families ever to be found in such resonant configurations. After eliminating likely interlopers, the families' ages were 4.90 ± 1.60 and 5.10 ± 1.51 Myr, respectively.

We then compute resonant proper elements appropriate for both families, and estimated the initial ejection velocity field parameters with methods described in Section 7 for the two groups. We found $V_{EJ} = 10^{+11}_{-1}$ m s^{-1} for the 5507 and $V_{EJ} = 20^{+1}_{-4}$ m s^{-1} for the 5507 and 170 776 families, respectively.

Prior to this work, the only young asteroid families known to have all members in secular resonant configurations were the 633 Zelima family in the z_1 secular resonance (Tsirvoulis 2019; Carruba & Ribeiro 2020), which is a sub-family of the larger Eos family, and the 12 988 TiffanyKapler in the ν_6 secular resonance (Carruba et al. 2022b). The two families identified in this work bring this total up to four. The orbital distribution of these four families in the $(a, \sin(i))$ plane is shown in the left panel of Fig. 20. The right panel of Fig. 20 shows the estimated parent body radiuses as a function of the age estimates. While the formation of the Zelima asteroid family is a rather unlikely event, families like those of (170 776) (2004 CA_{95}) are expected to have been much more common occurrences in the latest 10 Myr (see Section 8). We expect that methods like those applied in this work will allow detecting many more of these young groups, allowing us to better understand the mechanisms behind the formation of asteroid families.

CODE AVAILABILITY

The deep learning and machine learning codes used in this work are available in the GitHub repository under a MIT public license (*https://github.com/valeriocarruba/CNN-Optimization*, *https://github.com/valeriocarruba/Machine-learning-classification-of-new-asteroid-families-members*). All codes were written in PYTHON (https://www.python.org), using version 3.10.7 of the PYTHON interpreter, and the following libraries: NUMPY (*https://numpy.org/*, Oliphant (2006), version 1.23.5), PANDAS (*https://pandas.pydata.org/*, McKinney (2010), version 2.0.3), MATPLOTLIB (*https://matplotlib.org/*, Hunter (2007), version 3.7.1), SCIKIT-LEARN (*https://scikit-learn.org/stable/*, Pedregosa et al. (2011), version 1.3.0), IMBLEARN (*https://imbalanced-learn.org/stable/*, Lemaître, Nogueira & Aridas (2017), version 0.11.0), tensorflow (*https://www.tensorflow.org/*, Abadi et al. (2015), version 2.12.0), and KERAS (*https://keras.io/*, Chollet et al. (2015), version 2.12.0).

The source code for the symplectic integrator used for the numerical simulation of the asteroid orbits is part of the SWIFT package, that can be obtained at *https://www.boulder.swri.edu/ hal/swift.html*.

Any other codes or data presented in this paper can be obtained from the corresponding author upon reasonable request.

SUPPLEMENTARY MATERIAL 1: QUOTED PAPERS ON ASTEROIDS' PHYSICAL PROPERTIES

Data and metodologies used for obtaining information on the asteroid groups studied in this work were obtained from Rivkin (2012), Sergeyev & Carry (2021), Tinaut-Ruano et al. (2023), Mahlke, Carry & Mattei (2022b), DeMeo & Carry (2013), Milani et al. (2014), Carvano et al. (2010), Jasmim et al. (2013), Popescu et al. (2018), Sergeyev et al. (2022), Mahlke, Carry & Mattei (2022b), Vinogradova (2019), Erasmus et al. (2018), Erasmus et al. (2019), Schemel & Brown (2021), and Berthier et al. (2022a).

ACKNOWLEDGEMENTS

We are grateful to the reviewer of this paper, Dr Jorge Correa-Otto, for helpful comments and suggestions that helped to improve the quality of this paper. This work was supported by the 'Preparing for Astrophysics with LSST Program', funded by the Heising Simons Foundation through grant 2021–2975, and administered by Las Cumbres Observatory. We would like to thank the Brazilian National Research Council (CNPq, grants 301577/2017-0, 153683/2018-0). ZK acknowledges support from the Serbian Academy of Sciences and Arts through the project F-187. FR is grateful for the support from CNPq, grant 306009/2019-6. RCD thanks to the São Paulo Research Foundation (FAPESP, grant 2016/024561-0) and the Financier of Studies and Projects (Finep, grant 0527/18). GC acknowledges support from the Coordination for the Improvement of Higher Level Personnel (CAPES, Finance Code 001). MVFL is thankful for the support from FAPESP, grant 2022/14241-9. We are grateful for the use of data from the Asteroid Dynamics Site (AstDyS) (*https://newton.spacedys.com/astdys/*, Knežević & Milani (2003)). This work has made use of data from the European Space Agency (ESA) mission *Gaia* (https://www.cosmos.esa.int/gaia), processed by the *Gaia* Data Processing and Analysis Consortium (DPAC, https://www.cosmos.esa.int/web/gaia/dpac/consortium). Funding for the DPAC has been provided by national institutions, in particular the institutions participating in the *Gaia* Multilateral Agreement. Additionally, we acknowledge the invaluable contribution of data products from the *Wide-field Infrared Survey Explorer* (WISE) and Near-Earth Objects (NEOWISE), which are a joint project of the University of California, Los Angeles, and the Jet Propulsion Laboratory/California Institute of Technology, funded by the National Aeronautics and Space Administration. Finally, this research has also made use of data and/or services provided by the International Astronomical Union's Minor Planet Center. This is a publication from the MASB (Machine-learning applied to small bodies, https://valeriocarruba.github.io/Site-MASB/) research group. Questions on this paper can also be sent to the group email address: *mlasb2021@gmail.com*.

DATA AVAILABILITY

Data on labels for asteroids affected by the $2\nu_6 - \nu_5$ and $3\nu_6 - 2\nu_5$ resonances and our best-performing CNN model weigths, as well as a set of images of resonant angles for multi-opposition asteroids affected by the $2\nu_6 - \nu_5$ resonance are available at this MASB repository:

https://drive.google.com/drive/u/1/folders/1QmMsiwMXU7MtnIltBlmwMF_pam1aQTVY

The data that support the plots within this paper and other findings of this study are either available in the paper and in its supplementary materials tables, or are available from the corresponding author upon reasonable request.

REFERENCES

Abadi M. et al., 2015, TensorFlow: Large-Scale Machine Learning on Heterogeneous Systems, available at: https://tensorflow.org/
Beaugé C., Roig F., 2001, Icarus, 153, 391
Bendjoya P., Zappalà V., 2002, in, Asteroids III. Tucson, Arizona Univ. Press, p. 613
Benz W., Asphaug E., 1999, Icarus, 142, 5
Berthier J., Carry B., Mahlke M., Normand J., 2022a, SsODNet: The Solar system Open Database Network, available at: https://arxiv.org/abs/2209.10697
Berthier J., Carry B., Mahlke M., Normand J., 2022b, A&A, x, x1
Bottke W. F., Vokrouhlický D., Brož M., Nesvorný D., Morbidelli A., 2001, Science, 294, 1693
Bottke W. F., Durda D. D., Nesvorný D., Jedicke R., Morbidelli A., Vokrouhlický D., Levison H., 2005, Icarus, 175, 111
Brož M., Morbidelli A., 2013, Icarus, 223, 844
Brož M., Vokrouhlický D., 2008, MNRAS, 390, 715
Bus S. J., Binzel R. P., 2002, Icarus, 158, 146
Carruba V., 2009, MNRAS, 395, 358
Carruba V., 2010, MNRAS, 408, 580
Carruba V., Morbidelli A., 2011, MNRAS, 412, 2040
Carruba V., Ribeiro J. V., 2020, Planet. Space Sci., 182, 104810
Carruba V., Domingos R., Nesvorný D., Roig F., Huaman M., Souami D., 2013, MNRAS, 433, 2075
Carruba V., Vokrouhlický D., Novaković B., 2018, Planet. Space Sci., 157, 72
Carruba V., Spoto F., Barletta W., Aljbaae S., Fazenda Á. L., Martins B., 2020, Nat. Astron., 4, 83
Carruba V., Aljbaae S., Domingos R. C., Barletta W., 2021, MNRAS, 504, 692
Carruba V., Aljbaae S., Caritá G., Domingos R. C., Martins B., 2022a, Celest. Mech. Dyn. Astron., 134, A59
Carruba V., Aljbaae S., Domingos R. C., Huaman M., Martins B., 2022b, MNRAS, 514, 4803
Carvano J. M., Hasselmann P. H., Lazzaro D., Mothé-Diniz T., 2010, A&A, 510, A43
Chollet F. et al., 2015, Keras, available at: https://github.com/keras-team/keras
Cibulková H., Brož M., Benavidez P. G., 2014, Icarus, 241, 358
DeMeo F. E., Carry B., 2013, Icarus, 226, 723
DeMeo F. E., Binzel R. P., Slivan S. M., Bus S. J., 2009, Icarus, 202, 160
Erasmus N., McNeill A., Mommert M., Trilling D. E., Sickafoose A. A., van Gend C., 2018, ApJS, 237, 19
Erasmus N., McNeill A., Mommert M., Trilling D. E., Sickafoose A. A., Paterson K., 2019, ApJS, 242, 15
Ester M., Kriegel H.-P., Sander J., Xu X., 1996, in Proceedings of the Second International Conference on Knowledge Discovery and Data Mining (KDD-96)AAAI press, Portlland, Oregon, USA. p. 226
Farinella P., Davis D. R., 1992, Icarus, 97, 111
Ferraz-Mello S., 1981, AJ, 86, 619
Gaia Collaboration, 2022, A&A
He K., Zhang X., Ren S., Sun J., 2015, Deep Residual Learning for Image Recognition, available at: https://arxiv.org/abs/1512.03385
Huaman M., Carruba V., Domingos R. C., Aljbaae S., 2017, MNRAS, 468, 4982
Hunter J. D., 2007, Comput. Sci. Eng., 9, 90
Ivezić Ž. et al., 2001, AJ, 122, 2749

Jasmim F. L., Lazzaro D., Carvano J. M. F., Mothé-Diniz T., Hasselmann P. H., 2013, A&A, 552, A85
Jones R. L., Jurić M., Ivezić Z., 2015, Proc. Int. Astron. Union, 10, 282
Knežević Z., 2022, Serb. Astron. J., 204, 1
Knežević Z., Milani A., 2003, A&A, 403, 1165
Lazzaro D., Angeli C. A., Carvano J. M., Mothé-Diniz T., Duffard R., Florczak M., 2004, Icarus, 172, 179
Lemaître G., Nogueira F., Aridas C. K., 2017, J. Machine Learn. Res., 18, 1
Mahlke M., Carry B., Denneau L., 2021, Icarus, 354, 114094
Mahlke M., Carry B., Mattei P.-A., 2022a, A&A, 665, A26
Mahlke M., Carry B., Mattei P. A., 2022b, A&A, 665, A26
Mainzer A. et al., 2012, ApJ, 745, 7
Masiero J. R., Mainzer A. K., Grav T., Bauer J. M., Cutri R. M., Nugent C., Cabrera M. S., 2012, ApJ, 759, L8
Masiero J. R., Mainzer A. K., Bauer J. M., Grav T., Nugent C. R., Stevenson R., 2013, ApJ, 770, 7
McKinney W., 2010, Proc. 9th Python Sci. Conf., 445 (1), 51
Milani A., Knežević Z., 1990, Celest. Mechan. Dyn. Astron., 49, 347
Milani A., Knežević Z., 1992, Icarus, 98, 211
Milani A., Nobili A. M., 1988, Celest. Mech., 43, 1
Milani A., Cellino A., Knežević Z., Novaković B., Spoto F., Paolicchi P., 2014, Icarus, 239, 46
Milani A., Knežević Z., Spoto F., Cellino A., Novaković B., Tsirvoulis G., 2017, Icarus, 288, 240
Morbidelli A., 1993, Icarus, 105, 48
Murray C., Dermott S., 1999, Solar System Dynamics. Cambridge Univ. Press, Cambridge
Nesvorný D., Bottke William F. J., Dones L., Levison H. F., 2002, Nature, 417, 720
Nesvorný D., Brož M., Carruba V., 2015, in, Asteroids IV. Tucson, Univ. of Arizona, p. 297
Novaković B., Vokrouhlický D., Spoto F., Nesvorný D., 2022, Celest. Mech. Dyn. Astron., 134, 34
Oliphant T. E., 2006, Trelgol Publishing, A guide to Numpy, 1, 140
Parker A., Ivezić Ž., Jurić M., Lupton R., Sekora M. D., Kowalski A., 2008, Icarus, 198, 138
Pedregosa F. et al., 2011, J. Mach. Learn. Res., 12, 2825
Popescu M., Licandro J., Carvano J. M., Stoicescu R., de León J., Morate D., Boacă I. L., Cristescu C. P., 2018, A&A, 617, A12
Pravec P. et al., 2010, Nature, 466, 1085
Radović V., 2017, MNRAS, 471, 1321
Radović V., Novaković B., Carruba V., Marčeta D., 2017, MNRAS, 470, 576
Rivkin A. S., 2012, Icarus, 221, 744
Roig F., Nesvorný D., 2020, AJ, 160, 110
Ryan E. L., Woodward C. E., 2010, AJ, 140, 933
Schemel M., Brown M. E., 2021, ApJ, 2, 40
Sergeyev A. V., Carry B., 2021, A&A, 652, A59
Sergeyev A. V., Carry B., Onken C. A., Devillepoix H. A. R., Wolf C., Chang S. W., 2022, A&A, 658, A109
Simonyan K., Zisserman A., 2014, preprint (arXiv:1409.1556)
Spoto F., Milani A., Knežević Z., 2015, Icarus, 257, 275
Szegedy C. et al., 2015, in Proceedings of the IEEE Conference on Computer Vision and Pattern Recognition, Scientific Research Publishing, Wuhan, China,p. 1
Tinaut-Ruano F. et al., 2023, A&A, 669, L14
Tsirvoulis G., 2019, MNRAS, 482, 2612
Usui F. et al., 2011, PASJ, 63, 1117
Vinogradova T. A., 2019, MNRAS, 484, 3755
Vokrouhlický D., Brož M., Bottke W. F., Nesvorný D., Morbidelli A., 2006a, Icarus, 182, 118
Vokrouhlický D., Brož M., Bottke W. F., Nesvorný D., Morbidelli A., 2006b, Icarus, 183, 349
Wetherill G. W., 1967, J. Geophys. Res., 72, 2429
Zappala V., Cellino A., Farinella P., Knežević Z., 1990, AJ, 100, 2030

This paper has been typeset from a TEX/LATEX file prepared by the author.